https://doi.org/10.5194/wes-2026-208
Preprint. Discussion started: 5 November 2026
© Author(s) 2026. CC BY 4.0 License.

eawe european academy of wind energy
Open Access WIND ENERGY SCIENCE DISCUSSIONS

The Impact of Atmospheric Gravity Waves on Turbine Scale Flows

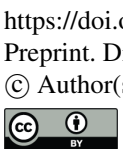
Timothy Rafferty[1] and Christopher R. Vogel[1]
[1]Department of Engineering Science, University of Oxford, Oxford, OX1 3PJ, United Kingdom
Correspondence: Timothy Rafferty (timothy.rafferty@eng.ox.ac.uk)

Abstract. Modern, taller, wind turbines can now interact with the geostrophic layers of the atmosphere, triggering the formation of gravity waves. However, there remains limited understanding of how these waves interact with flows at the turbine scale. Using Large Eddy Simulations (LES) of a wind turbine represented by an actuator line model, the impact of turbine generated gravity waves on the wake dynamics, blade loading and power production was investigated. The waves were found to induce a sinusoidal variation in wake width in both the vertical and horizontal directions. Wake recovery was observed to be non-monotonic, with an inverse relationship between the peaks and troughs in velocity deficit and the waves aloft. An evaluation of the turbulent and mean energy budget terms of the turbine wake showed the gravity waves had relatively little impact on the instantaneous flow. The effect of turbine lateral spacing was also investigated by varying the domain width. The strength of the waves triggered, and consequently the wave induced wake variations, was found to be negatively correlated with the lateral spacing. Furthermore, a wave-induced upstream deceleration was observed in all cases. The magnitude of the deceleration decreased with wave strength, with both the wave strength and deceleration asymptotically approaching non-zero values as lateral spacing increased. The simulations in this work demonstrate that waves can be initiated despite only modelling one turbine, offering a lower computational cost methodology for investigating gravity waves. This approach also suggests that relatively small clusters of turbines may be capable of triggering gravity waves, rather than just the large wind farms of 100+ turbines which have been commonly the focus of previous gravity wave research. Finally, simulations with turbulent and uniform inflows showed good agreement in the gravity waves produced and the resulting wave-induced flow variations. The consistency between the inflow cases, further supports the gravity waves and their impacts being relatively independent of the instantaneous variations in the turbine-scale flow field.

1 Introduction

With the growth of offshore wind farms in both turbine number and size, the farms are now interacting significantly with meso-scale atmospheric flows (Porté-Agel et al., 2020; Veers et al., 2022; Stevens and Meneveau, 2017). Therefore, understanding the impact of meso-scale phenomena such as Atmospheric Gravity Waves (AGWs) on turbine and farm aerodynamics is increasingly important. AGWs are triggered by the vertical displacement of thermally stratified air, which induces a restoring buoyancy force. The wave forms and propagates through the interaction between the inertia of the displaced air parcel and the buoyancy forcing (Nappo, 2012). Whilst these waves do propagate in time and space through a Lagrangian frame of reference, they appear stationary to an Eulerian observer. The initial perturbation which triggers the waves can be caused by a resistance

https://doi.org/10.5194/wes-2026-208
Preprint. Discussion started: 5 November 2026
© Author(s) 2026. CC BY 4.0 License.



eawe european academy of wind energy
Open Access WIND ENERGY SCIENCE DISCUSSIONS

to the flow, such as a mountain range or tree canopy (Wallace and Hobbs, 2006). Smith (2010) predicted, through analytical models, that sufficiently large wind farms could also present the necessary level of resistance to the flow, deflecting the flow upstream of the farm vertically and subsequently triggering gravity waves. This scenario has been further explored by several authors using Large Eddy Simulations (LES) to investigate offshore wind farm performance under AGW conditions (Allaerts and Meyers, 2017; Lanzilao and Meyers, 2022; Stipa et al., 2024b; Maas, 2023a; Wu and Porté-Agel, 2017).

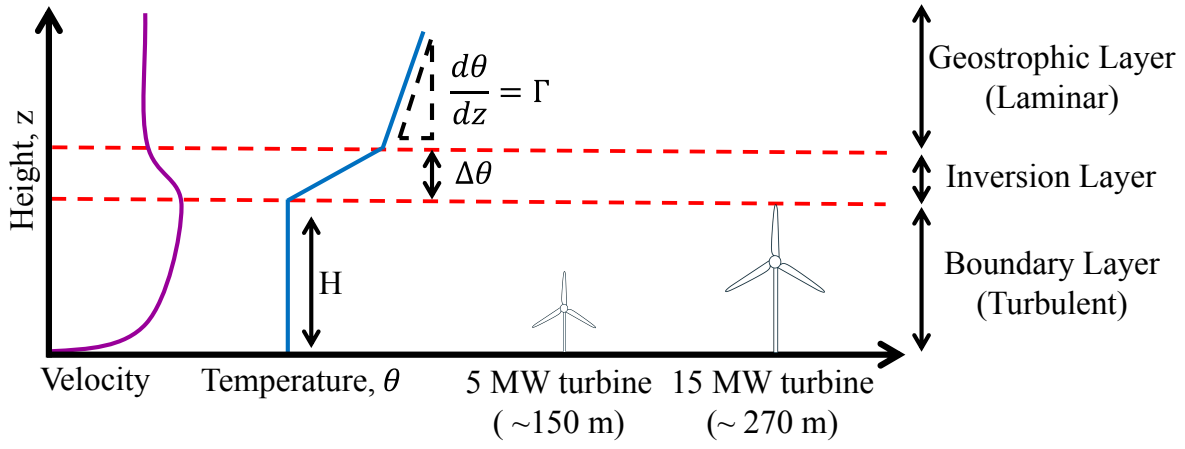


Figure 1. The Conventionally Neutral Boundary Layer (CNBL) velocity and corresponding temperature profiles with a comparison to typical wind turbine dimensions.

The atmospheric boundary layer in the North Sea can often be classed as a Conventionally Neutral Boundary Layer (CNBL) (Allaerts and Meyers, 2015; Lanzilao and Meyers, 2024). The CNBL consists of velocity and temperature profiles as indicated in Fig. 1 (Stull, 2015). The CNBL consists of three key regions: the boundary layer, which is characterised by a turbulent flow with a sheared profile and a uniform temperature profile; the inversion layer, where temperature increases with height; and the geostrophic layer, which is characterised by homogenous flow and a temperature gradient an order of magnitude weaker than that of the inversion layer (Lanzilao and Meyers, 2024). The maximum height of a typical 15 MW turbine is much closer to the inversion layer than older 5 MW ones, making perturbations to the inversion layer more likely (Jonkman et al., 2009; Gaertner et al., 2020).

Previous simulations investigating AGWs have employed these CNBL inflow profiles together with either 5 MW or 10 MW turbines (Allaerts and Meyers, 2017; Lanzilao and Meyers, 2022; Stipa et al., 2024b; Maas, 2023a; Wu and Porté-Agel, 2017). In simulations there are a wide range of spatial scales to resolve, from rotors with diameters of 100 to 250 m, to gravity waves with typical wavelengths of 2 to 10 km, and wind farms spanning 10 to 20 km. Capturing the full range of scales would make the computational expense of the LES prohibitive. Therefore, the existing literature has primarily focussed on the interactions between AGWs and flow at the farm scale.

https://doi.org/10.5194/wes-2026-208
Preprint. Discussion started: 5 November 2026
© Author(s) 2026. CC BY 4.0 License.



eawe european academy of wind energy
Open Access WIND ENERGY SCIENCE DISCUSSIONS

The LES simulations of Allaerts and Meyers (2017) showed that farms under CNBL conditions could trigger both a trapped wave propagating horizontally in the inversion layer and an internal wave propagating through the geostrophic layer. Despite propagating only in the stratified geostrophic layers, the waves were observed to influence the pressure field surrounding the entire farm, impacting farm-scale flows within the boundary layer.

A key result of the AGW-induced modifications to the pressure field was flow deceleration in the boundary layer upstream of the farm. Upstream deceleration of flow has also been observed in simulations for wind farms under neutral conditions and confirmed with field and experimental measurements (Strickland and Stevens, 2022; Bleeg et al., 2018). The flow approaching the farm decelerates due to the resistance presented by the turbines, with flow being diverted laterally around and above the farm. This is sometimes referred to as the farm or global blockage effect in the literature, although it is noted that the concept of blockage has also been used to describe the geometric ratio of turbine swept area to surrounding flow passage area, for example in a wind tunnel or confined flow. In the AGW cases, the upstream deceleration impact on the first row power production, relative to a rotor in isolation, was observed to be more than 15 times that observed for farms under neutral flows (Wu and Porté-Agel, 2017; Lanzilao and Meyers, 2024). Thus, in AGW cases the deceleration observed has often been termed a wave-induced global blockage effect. However, as both the AGW and wave-free simulations reported in the literature experience farm blockage, it remains unclear whether AGWs simply magnify the farm deceleration mechanism seen in the wave-free cases, or whether the waves are a separate mechanism that further compounds the observed upstream deceleration as suggested by Lanzilao and Meyers (2024).

In addition to the impact of AGWs on the front row of a wind farm, it has been shown that AGWs can influence the flow experienced by turbines at the farm outlet (Wu and Porté-Agel, 2017; Lanzilao and Meyers, 2024). In some AGW simulations, the final farm rows outperformed rows in the middle of the farm, contrary to the typical pattern of farm power production. Differences in farm wake length have also been observed between AGW and wave-free cases. Allaerts and Meyers (2017) performed an energy budget analysis on the farm scale to evaluate the AGW mechanism leading to the observed pattern in turbine performance. The budget analysis demonstrated that the energy lost in the boundary layer, leading to the upstream deceleration, was contained within the AGW's pressure field and partially redistributed at the farm outlet. Their work illustrated the importance of resolving AGWs for accurate power predictions, as deep into farms turbine performance is often governed by the vertical kinetic energy flux from the upper atmosphere rather than the boundary layer flow field (Stevens and Meneveau, 2017).

Lanzilao and Meyers (2024) extensively investigated the relationship between the CNBL thermal parameters and the AGWs that are triggered. The strength of the AGWs was quantified through the extent of the inversion layer displacement and the amplitude of the perturbations to the geostrophic layer flow fields amongst other factors. Lanzilao and Meyers (2024) showed that the geostrophic stratification (Γ), inversion layer strength ($\Delta\theta$) and inversion layer height (H) all impacted the strength of the triggered waves. This work among others (Stipa et al., 2024b; Maas, 2023a) used a farm of a finite size and by doing so demonstrated that the AGW effects and trends observed in the original LES simulations of Allaerts and Meyers (2017), where a farm with infinite width had been used, were still valid (Allaerts and Meyers, 2017).

https://doi.org/10.5194/wes-2026-208
Preprint. Discussion started: 5 November 2026
© Author(s) 2026. CC BY 4.0 License.



eawe european academy of wind energy
Open Access WIND ENERGY SCIENCE DISCUSSIONS

Previous studies have demonstrated that gravity waves can have a significant influence on both farm power production and the flow profile around the farm. However, the use of low-fidelity actuator disk models for turbine representation on coarse meshes (20 to 30 m resolution) limited the analysis to only the farm scale (Allaerts and Meyers, 2017; Stipa et al., 2024b; Lanzilao and Meyers, 2024; Maas, 2023b). Actuator disks do not capture blade-induced coherent wake structures such as tip vortices, and can under-predict wake turbulence intensity and velocity deficits (Rafferty and Vogel, 2026; Revaz and Porté-Agel, 2021; Wu and Porté-Agel, 2011; Li et al., 2022). Consequently, the ability of simulations using the actuator disk model to accurately predict the flow at the turbine-scale, can be limited. Furthermore, the work in the literature has only used farms with one spacing distance between turbines and regular farm shapes, limiting the understanding of how intra-farm flow dynamics impact the AGWs (Allaerts and Meyers, 2017; Stipa et al., 2024b; Lanzilao and Meyers, 2024; Maas, 2023b).

As previously mentioned, the primary reason limiting the analysis to only evaluating the farm scale flows, is the high computational costs of such simulations. Along with a wide range of spatial scales to resolve, the simulations have to model 100+ turbines in domains of 10s of kilometres in size as to accommodate the farm, its wake and to fully resolve the gravity waves. However, given the simulations of infinitely wide farms effectively captured AGW interactions, it calls into question whether the finite farm simulations of 100+ turbines, and their associated computational costs, are necessary for evaluating the underlying physics behind the AGWs and their impacts. Furthermore, in cases with an infinite farm width there was an over prediction of AGW impacts due to the absence of a lateral bypass around the farm (Allaerts and Meyers, 2017; Wu and Porté-Agel, 2017; Lanzilao and Meyers, 2024). This exaggeration of AGW characteristics may in fact be useful for isolating AGW-induced phenomena from the many other factors in atmospheric flows such as the Coriolis force, turbulence and sheared profiles.

It is important to understand how atmospheric phenomena influence flow across different spatial scales, as the inclusion of more realistic atmospheric inflows which have turbulence, sheared profiles and thermal stratification have been previously shown to significantly impact the turbine scale flow (Abkar and Porté-Agel, 2015; Wu and Porté-Agel, 2012). In particular, wake recovery, meandering and blade loading have all been found to be sensitive to atmospheric parameters (Porté-Agel et al., 2020). It is therefore hypothesised that AGWs could impact upon turbine scale flows as well. This hypothesis is further supported by the AGW length scale being of similar magnitude to the wake length of a large rotor. Consequently, a better understanding of the underlying physics of the waves is needed, through computationally feasible simulations, that determine whether, and by what mechanisms, AGWs impact the turbine scale.

By simulating a turbine with a higher fidelity Actuator Line (AL) model to capture discrete blade effects and varying the lateral turbine spacing, this work aims to build on the literature in evaluating three key areas. First, determining if AGWs impact the flow on the turbine scale, with a particular focus on how the wake dynamics are altered. Second, evaluating the nature of the AGW-induced upstream deceleration to determine if it is independent of the farm blockage effect. Finally, assessing the role of lateral turbine spacing in impacting how AGWs are triggered and subsequently affect the rotor dynamics. Assessing different lateral spacings will also identify if intra-farm design could alter AGW interactions and to what extent the two are correlated.

https://doi.org/10.5194/wes-2026-208
Preprint. Discussion started: 5 November 2026
© Author(s) 2026. CC BY 4.0 License.



eawe european academy of wind energy
Open Access WIND ENERGY SCIENCE DISCUSSIONS

2 Methodology

To answer the posed research questions, this study simulated a wind turbine under CNBL conditions using the precursor-successor method as shown in Fig. 2. The method develops a turbulent stratified offshore boundary layer flow in an empty domain, the precursor. The precursor flow field subsequently becomes the inflow conditions to a second domain, the successor, which contains the wind turbine being simulated.

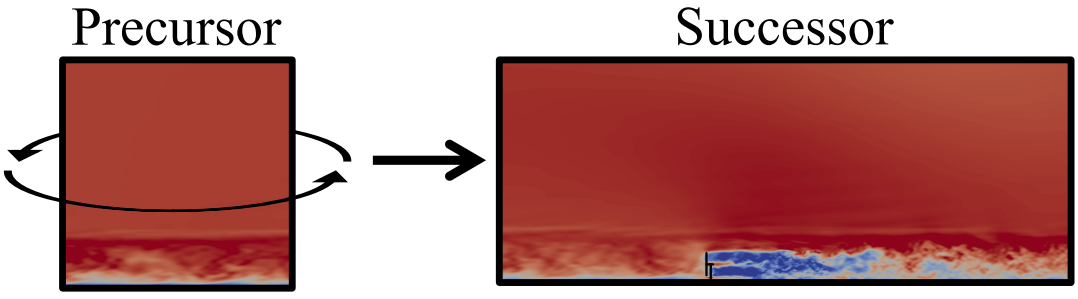


Figure 2. An illustration of the overall simulation methodology. A precursor domain with cyclic conditions on the left hand side generates the flow field for the successor on the right hand side. The successor contains a wind turbine which has been illustrated.

The open source National Laboratory of the Rockies (NLR, formerly NREL) solver Simulator fOr Wind Farm Applications (SOWFA) 6 was chosen for these LES simulations. SOWFA-6 is the updated version of SOWFA, which has previously been used extensively in the literature (Churchfield et al., 2012; Fleming et al., 2014; Ning et al., 2021; Doubrawa et al., 2019; Scott et al., 2023). SOWFA-6 was directly used with the open source Computational Fluid Dynamics (CFD) code OpenFOAM v2012. Comparisons of SOWFA-6 with other codes such as AMR-Wind have been made in the literature and they show strong agreement in the CNBL flows produced (Dammann et al., 2025). The repository for SOWFA-6 can be found at NLR (2022) and will hereafter be referred to as SOWFA. The details of this flow solver and the associated simulation setup for both the precursor and successor are covered in the following sections.

2.1 Governing Equations

The spatially filtered Navier Stokes equations for mass conservation, momentum transport and potential temperature transport solved by SOWFA are given by Equations 1, 2 and 3 respectively:

$$\frac{\partial \tilde{u}_i}{\partial x_i} = 0 \tag{1}$$

$$\frac{\partial \tilde{u}_i}{\partial t} + \frac{\partial}{\partial x_j}\left(\tilde{u}_j \tilde{u}_i\right) = -2\varepsilon_{i3k}\Omega_3 \tilde{u}_k - \frac{\partial p'}{\partial x_i} - \frac{\partial}{\partial x_i}\langle\frac{p_0(x,y)}{\rho_0}\rangle - \frac{\partial}{\partial x_j}\left(\tau_{ij}^D\right) - g_3 z \frac{\partial}{\partial x_i}\left(\frac{\rho_b}{\rho_0}\right) + F_i \tag{2}$$

$$\frac{\partial \tilde{\theta}}{\partial t} + \frac{\partial}{\partial x_j}\left(\tilde{u}_j \tilde{\theta}\right) = -\frac{\partial}{\partial x_j}\left(q_j\right) \tag{3}$$

https://doi.org/10.5194/wes-2026-208
Preprint. Discussion started: 5 November 2026
© Author(s) 2026. CC BY 4.0 License.



eawe european academy of wind energy
Open Access WIND ENERGY SCIENCE DISCUSSIONS

where the time averaged velocity and temperature are given by $\bar{u}$ and $\bar{\theta}$. The tilde (˜) indicates a spatially filtered quantity. The term ε_{ijk} is the Levi-Civita symbol and $\langle\rangle$ denotes a horizontal average. The terms p, t, ρ and g are the pressure, time, density and gravitational acceleration respectively. Notably the 3rd, 7th and 8th terms in Eq. 2 are additional to the standard PIMPLE solver momentum transport equation. The 3rd term represents the Coriolis force to account for planetary rotation, where Ω is the rotation rate of the Earth. The 7th term represents the buoyancy forcing, where ρ_0 is the reference density. The 7th term couples the momentum and temperature transport equations utilising the Boussinesq approximation:

$$\frac{\rho_b}{\rho_0} = 1 - \frac{\tilde{\theta} - \theta_0}{\theta_0} \tag{4}$$

where θ_0 is a reference temperature. Finally, the 8th term represents additional forcing from damping regions and the wind turbine.

In SOWFA the pressure is split into its fluctuating or modified pressure given by Eq. 5 and the averaged component or background driving pressure gradient $\frac{\partial}{\partial x_i}\langle\frac{p_0(x,y)}{\rho_0}\rangle$. As part of the fluid stress tensor (τ_{ij}) is implicitly included in the modified pressure shown in Eq. 5, the fourth term in the momentum equation becomes just the divergence of the deviatoric stress tensor.

$$p' = \frac{\tilde{p}}{\rho_0} - \frac{\rho_b}{\rho_0} g_j x_j - \langle\frac{p_0(x,y)}{\rho_0}\rangle + \delta_{ij}\frac{\tau_{kk}}{3} \tag{5}$$

The background driving pressure gradient is not solved for in SOWFA and is instead adjusted in the precursor at each time step so that a specified horizontal wind speed and direction at the turbine hub height can be achieved. In the successor this background pressure term is set based on the value at the equivalent time step of the precursor.

For the sub-grid scale turbulence modelling, the standard OpenFOAM Smagorinsky model was used with van Driest near wall damping. This damping along with a 10 m vertical cell resolution, as suggested by NLR, was chosen to capture the law of the wall scaling. The exact best practice for treating near-wall flow, however, is dependent on multiple factors such as the mesh and solver, making it an open discussion in the literature which goes beyond the scope of this work (Brasseur and Wei, 2010; Porté-Agel et al., 2000; Khanna and Brasseur, 1997).

For the temporal scheme a second order implicit backward scheme was used and for the spatial domain a second order central difference scheme was used. These governing equations and assumptions are widely used for simulating wind farms in CNBL flows; further information on them can be found in the literature for SOWFA (Churchfield et al., 2012) and more generally in the literature on pressure handling (Deardorff, 1972; Moeng, 1984), the Coriolis force (Lanzilao and Meyers, 2024; Wyngaard, 2010) and the Boussinesq approximation (Maas, 2023a; Spiegel and Veronis, 1960).

2.2 Boundary Conditions

The boundary conditions used in this work are the standard ones implemented in SOWFA simulations for CNBL flows and will be briefly discussed, for further information see Churchfield et al. (2012).

https://doi.org/10.5194/wes-2026-208
Preprint. Discussion started: 5 November 2026
© Author(s) 2026. CC BY 4.0 License.



eawe european academy of wind energy
Open Access WIND ENERGY SCIENCE DISCUSSIONS

2.2.1 Precursor

For the precursor, cyclic conditions were used for the lateral and streamwise boundaries so as to efficiently develop the flow. For the lower and upper boundaries shear stress, temperature, velocity and pressure conditions were implemented.

A zero stress condition was implemented on the upper boundary. On the lower boundary, a wall shear stress was implemented to simulate a sea surface-air interaction. For this, the Schumann wall model was used with the velocity being sampled from the cell centre next to the wall and the magnitude of the vertical flux of horizontal momentum, u_*^2, estimated using Monin-Obukhov similarity theory. This wall-stress modelling methodology is widely employed throughout the literature (Wu and Porté-Agel, 2017; Allaerts and Meyers, 2015; Lanzilao and Meyers, 2024).

For the velocity, a slip condition was applied at the upper boundary. At the lower boundary, the normal velocity was set to zero to enforce a no penetration condition, while the horizontal velocity was set such that the normal velocity gradient at the first cell centre was equal to that at the top of the first cell. The velocity of the first cell thereby provides a meaningful input to the sub-grid scale model.

For temperature, the upper boundary was set such that the gradient was equivalent to the thermal stratification of the geostrophic layer and for the lower boundary the temperature gradient was set to zero. Finally, fixed-flux pressure conditions were applied on the lower and upper boundaries to ensure consistency with the velocity conditions.

2.2.2 Successor

In the successor, the same boundary conditions were used as the precursor except in the streamwise direction. For the successor, the inflow boundary for velocity and temperature was set using a plane sampled from the precursor. For the outlet, an inlet-outlet condition was used for velocity and zero gradient condition for temperature to minimise AGW reflections. For pressure a fixed-flux pressure condition was used for the inlet and a zero gradient condition for the outlet. As the successor used cyclic lateral boundaries, the simulations replicate the middle wind turbine in an infinitely wide row with a lateral spacing equivalent to the domain width.

2.2.3 SOWFA Methodology Modifications

Whilst the standard precursor-successor method for SOWFA simulations was used, two additions were made to the solver.

First, the precursor was altered to remove geostrophic inertial oscillations. These temporal oscillations, which were found to have a magnitude of up to $3\,\mathrm{m\,s^{-1}}$, cause two issues for gravity wave simulations. First, they prevent the accurate calibration of the damping layers needed in an AGW simulation and second, as a result of the geostrophic velocity variation, the wavelength of the gravity waves becomes variable in the successor. The oscillations occur because the precursor is driven using a pressure gradient calibrated to a hub height velocity, so the geostrophic wind speed is not known *a priori*. Thus, a mismatch between the initialised and actual equilibrium geostrophic conditions leads to inertial oscillations in the geostrophic wind speed, as the momentum balance in the geostrophic layer takes the form of a classical linear undamped oscillator (Stipa et al., 2024b; Stull,

https://doi.org/10.5194/wes-2026-208
Preprint. Discussion started: 5 November 2026
© Author(s) 2026. CC BY 4.0 License.



eawe european academy of wind energy
Open Access WIND ENERGY SCIENCE DISCUSSIONS

2015). Although the oscillations can be a result of realistic planetary conditions, the oscillations here are artificially generated and therefore had to be removed.

Removal of the oscillations was done through the geostrophic damping method, developed by Stipa et al. (2024b), with the damping implemented only for part of the spin-up stage in precursor simulations. To aid with minimising the oscillations, the prescription of the initial conditions was also improved through implementing the methodology to predict the wind profile and geostrophic wind speed developed by Narasimhan et al. (2024). In keeping with the standard SOWFA setup, perturbations were still added in the near-wall velocity profile to promote faster turbulence initiation.

The second change to SOWFA was made to ensure the precursor created a flow which consistently had the desired temperature profile. With the precursor simulation being run for over 24 hours the temperature profile inevitably can evolve over time from the desired initial conditions. Therefore, the temperature controller developed by Stipa et al. (2024b), was also implemented for the precursor. The controller maintains a set temperature profile, therefore, allowing for both fair comparisons to be made within this work between simulations with varying setup and results from other codes or simulations in the literature.

2.3 Domain Setup

The domain size is defined by its length, width and height which in this work correspond to the x, y, and z axes. As cyclic lateral boundary conditions were used, the domain width was equivalent to the lateral spacing for a turbine row. For both the successor and precursor simulations this width was first set to three turbine diameters wide ($0.72\,\mathrm{km}$) for the initial wake analysis. The width was later changed to evaluate the impact of turbine lateral spacing within a row on the AGWs (see Section 3.3).

Unlike the choice of domain width, the choice of domain length and height were primarily selected to minimise artificial gravity wave reflections at the domain boundaries. Extensive recommendations exist in the literature for reducing reflections (Lanzilao and Meyers, 2024; Khan et al., 2025; Lanzilao and Meyers, 2023; Klemp and Lilly, 1978). These are summarised as:

1. Use wave damping regions of at least one wavelength size in the upper region of the domain and at both the inlet and outlet.

2. The domain should be large enough to resolve at least one wavelength in both streamwise directions and the vertical direction.

3. Use a damping region with a damping coefficient based on the Brunt-Väisälä frequency N given by equation $N = \sqrt{\Gamma \cdot g/\theta_0}$ where Γ is the thermal stratification of the geostrophic layer.

4. Use a gradient function to vary the strength of the damping layer, the shape of which can be tuned through preliminary simulations.

Following these recommendations, the domain for the successor took the layout shown in Fig. 3. With a domain length of five AGW wavelengths and a domain height of two AGW wavelengths above the boundary layer, the domain can sufficiently resolve at least one wavelength above, in front of, and behind the wind turbine. As shown in Fig. 3 the domain is set up to

https://doi.org/10.5194/wes-2026-208
Preprint. Discussion started: 5 November 2026
© Author(s) 2026. CC BY 4.0 License.



eawe european academy of wind energy
Open Access WIND ENERGY SCIENCE DISCUSSIONS

also include damping regions at the inlet, outlet and upper boundaries all one wavelength in size. Rayleigh damping (F_{Ray}) was chosen for these regions as it has been successfully used throughout the literature (Allaerts and Meyers, 2017; Stipa et al., 2024b; Khan et al., 2025). To vary the damping strength to a maximum at the boundaries, a cosine function given by Eq. 6 was used:

$$F_{Ray} = -C_d \cdot (U - U_{geo}) \cdot \frac{1}{2} \cdot (1 - cos(\frac{\pi \cdot (x_i - (L_b - L_d))}{L_d}) \tag{6}$$

where C_d is the damping coefficient, L_d is the damping layer length, L_b is the position of the boundary and U_{geo} is the geostrophic layer velocity. The damping coefficient C_d was set to 2 times the Brunt-Väisälä frequency and U_{geo} was prescribed based on the precursor simulation. For the lateral boundaries the cyclic condition ensures they are reflection free.

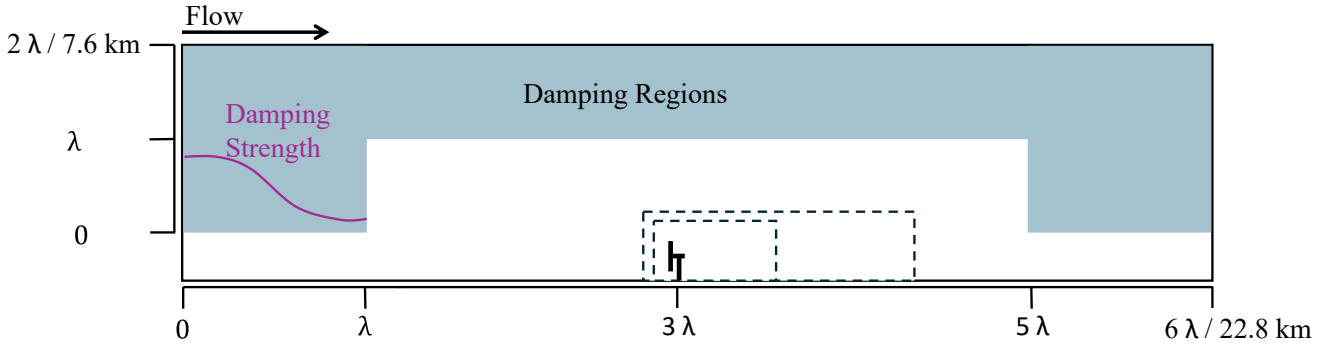


Figure 3. The domain used in the successor simulations with damping regions indicated by shading and dashed boxes to indicate mesh refinement regions around the turbine and wake. The axes are non-dimensionalised in terms of the gravity wave wavelength.

A reflection coefficient was used to evaluate the effectiveness of the simulation setup at reducing artificial wave reflections. The coefficient is found by decomposing the internal wave field into upward and downward propagating components and comparing the energy contained within each (Allaerts and Meyers, 2017; Taylor and Sarkar, 2007). A coefficient of less than 10 % has been agreed in the literature to be the limit for a simulation to be categorised as reflection free (Allaerts and Meyers, 2017; Khan et al., 2025). In the simulations for this work this value was less than 10 % for all cases and had an average of 7 %. For further information on the coefficient calculation see (Allaerts and Meyers, 2017), (Taylor and Sarkar, 2007) and (Khan et al., 2025).

Whilst the full length domain is required in the successor, there are no AGWs to resolve in the precursor, therefore, it can be shorter. A tiling approach was used as illustrated in Fig. 4, where the precursor is replicated multiple times and then combined to create the successor.

https://doi.org/10.5194/wes-2026-208
Preprint. Discussion started: 5 November 2026
© Author(s) 2026. CC BY 4.0 License.

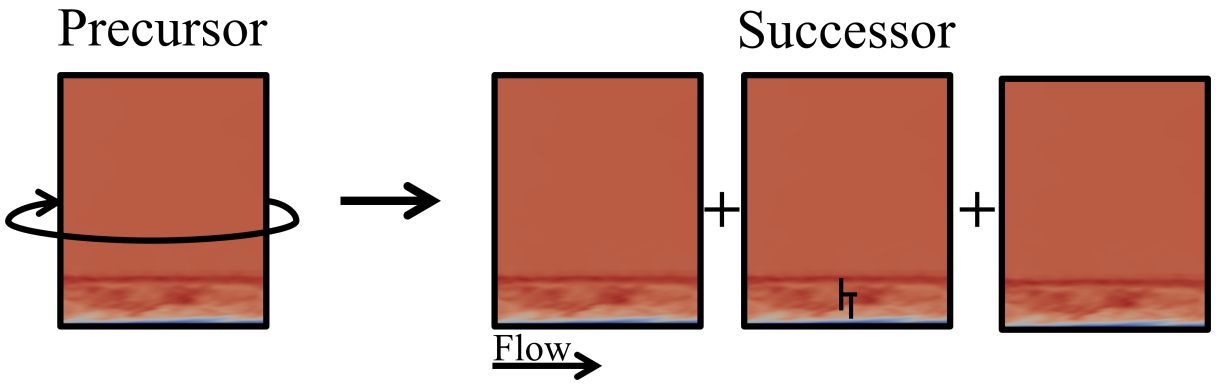


Figure 4. An illustration of the tiling method for extrapolating the precursor in the streamwise direction.

This tiling approach is conceptually similar to other tiling methods in the literature for expanding domains often in the spanwise directions (Stipa et al., 2024b; Lanzilao and Meyers, 2024; Stipa et al., 2024a; Sanchez Gomez et al., 2023; Han et al., 2023). The tiling method performs well for AGW simulations because the homogeneity of the geostrophic layer makes the layer insensitive to streamwise extrapolation. Furthermore, the long successor spin-up time ensures the flow has advected through at least one entire successor domain before data is collected.

To determine an appropriate length for the precursor domain, the relevant length scales of the flow were characterised. Using a simulation of an 11 km long precursor domain the maximum integral length scale of the flow was calculated following the two-point correlation method described by Pope (2000). The largest turbulent eddies were found near the wall and had a length on the order of 150 to 250 m. The other length scale of interest was that of the gravity waves, which have wavelengths on the order of kilometres. Therefore, the precursor domain streamwise length was set to be equivalent to one gravity wave wavelength. In addition, to avoid any turbulent structures becoming locked into the precursor and lasting for unrealistic timescales, the shifted boundary condition developed by Munters et al. (2016) was implemented for the precursor.

2.3.1 Mesh Size

A sensitivity study was carried out for the mesh, with a cell size of 20 m being selected for the horizontal (x,y) directions consistent with previous CNBL studies which used cell sizes in the range of 20 to 30 m (Allaerts and Meyers, 2017; Wu and Porté-Agel, 2017; Lanzilao and Meyers, 2024; Abkar and Porté-Agel, 2013). In the vertical direction (z) the mesh was stretched to ensure a small enough cell for accuracy in the boundary layer, where complex turbulent structures are present, while maintaining computational efficiency in the geostrophic layer, where the flow is homogeneous and in the damping regions being artificially forced. Therefore, the mesh was kept at a 10 m cell height up to twice the inversion layer height and then increased from 10 m to 60 m up to the damping layer and then over the damping region it was further stretched from 60 m to 300 m. This vertical size and stretching was informed by the same literature.

https://doi.org/10.5194/wes-2026-208
Preprint. Discussion started: 5 November 2026
© Author(s) 2026. CC BY 4.0 License.



eawe european academy of wind energy
Open Access WIND ENERGY SCIENCE DISCUSSIONS

Whilst this mesh size was adequate for the precursor, to effectively use the Actuator Line Method for the turbine representation, the mesh was further refined in the successor. This was done using two refinement regions as illustrated by the dashed boxes in Fig. 4. The outer region of size 22.5 D × 2 D × 2 D refined the mesh to a uniform 10 m size and started 2.5 D in front of the rotor. The inner region of size 9.5 D × 1.5 D × 1.96 D refined the mesh to 5 m (Δ_{cell}) and started 2 D in front of the rotor. This refinement provided 48 cells across the rotor plane. The length of the refinement boxes was chosen after initial testing to ensure the near wake of the turbine was captured at a 5 m resolution and the far wake at a 10 m resolution.

2.4 Atmospheric State and Precursor Flow Profiles

It was chosen to simulate flow conditions in the North Sea (latitude 55°) because this was the location of most European offshore wind farm development at the time of the work. Lanzilao and Meyers (2024) performed an extensive analysis of the ERA5 dataset to determine a typical range of thermal parameters for the North Sea wind profile. Using this range the CNBL parameters in Table 1 were chosen. These conditions also satisfy an additional condition of the inversion layer being above an approximate minimum height, calculated using Eq. 7:

$$H_{min} \approx A \cdot \frac{\theta_0}{g\Delta\theta} \cdot u_*^2 \tag{7}$$

where A is an empirical constant (~ 500). If the inversion layer height is above H_{min}, it should not evolve during the simulation (Allaerts and Meyers, 2015, 2017; Csanady, 1974).

For the shear stress lower boundary, the surface roughness z_0 was set to a typical value for the sea and resulted in a turbulence intensity of 3.9 % at hub height, 4.6 % at 90 m and 6.8 % at 30 m in the simulations (Stull, 2015). This level of turbulence is consistent with observations in the North Sea (Türk and Emeis, 2010). The inversion layer thickness was set to 100 m to be consistent with the range for other simulations in the literature (Stipa et al., 2024b; Lanzilao and Meyers, 2024). Finally, the hub height velocity was set to both fall within the typically simulated range and so that the 15 MW turbine was operating within the region for the optimal TSR (Gaertner et al., 2020).

Table 1. The key CNBL parameters.

Inversion Height H (m)	Hub Velocity ($\mathrm{m\,s^{-1}}$)	Stratification Γ ($\mathrm{K\,km^{-1}}$)	Inversion Strength $\Delta\theta$ (K)	Base Temperature θ_0(K)	Surface Roughness z_0 (m)
350	8	5	5	283	0.001

Velocity, temperature and wind angle profiles from the precursor simulations are given in Fig. 5. For comparison the profiles from precursors without temperature profiles and in one of the cases without a Coriolis forcing, are included. The profiles have been horizontally averaged over the domain and temporally averaged over 5000 s.

https://doi.org/10.5194/wes-2026-208
Preprint. Discussion started: 5 November 2026
© Author(s) 2026. CC BY 4.0 License.

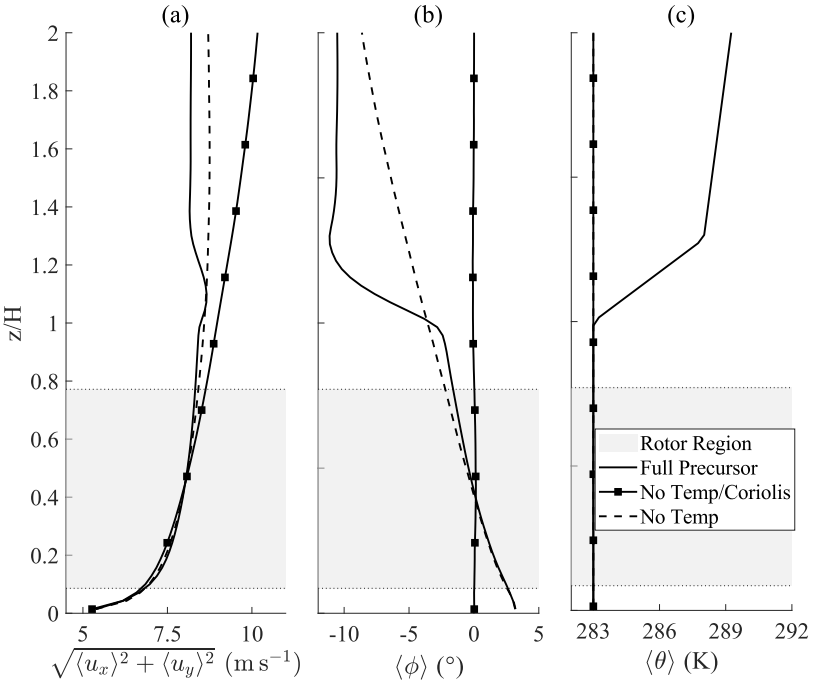


Figure 5. Time and spatially averaged vertical profiles of (a) wind speed (b) wind angle and (c) temperature, from precursor simulations. Three cases are included for comparison: a full precursor (-), a precursor without a temperature profile (- -) and a precursor without a temperature profile or the Coriolis forcing (■). The region within which the turbine operates is also indicated by the shading.

Notably, over the rotor plane the three velocity profiles in Fig. 5(a) are similar, but, above the maximum rotor height the profile is flatter for the cases with the Coriolis forcing. For the cases with the Coriolis forcing there is a variation in the wind angle over the rotor area with a magnitude of 4–5° (Fig 5(b)). In the full precursor a super-geostrophic jet also exists in the inversion layer, this is a common phenomenon in CNBL simulations when the inversion layer is low (Lanzilao and Meyers, 2024). Using Eq. 8 the atmospheric gravity wave wavelength can be calculated as

$$\lambda = \frac{2\pi \cdot U_{geo}}{N} \tag{8}$$

where U_{geo} is the geostrophic velocity taken from the precursor; AGWs in the successor were predicted (based on $U_{geo,x}$) to have a wavelength of approximately 3.8 km.

2.5 Wind Turbine and Actuator Line Model

The International Energy Agency 15 MW reference turbine was chosen to be simulated in this work (Gaertner et al., 2020). The 15 MW turbine is almost double the height of the NREL (now NLR) 5 MW reference turbine, so was expected to have a greater impact on the phenomena in the upper atmosphere than previous simulation work which used 5 or 10 MW turbines (Jonkman et al., 2009).

https://doi.org/10.5194/wes-2026-208
Preprint. Discussion started: 5 November 2026
© Author(s) 2026. CC BY 4.0 License.



eawe european academy of wind energy
Open Access WIND ENERGY SCIENCE DISCUSSIONS

The Actuator Line model (AL) was chosen for modelling the turbine to allow for detailed wake and blade load analysis to be carried out including characterising temporal variations. An in-house AL code, embedded in OpenFOAM, was used. The key model parameters, given in Table 2, were selected based on the recommendations in the literature and the Shen and Sørensen tip loss model was also used (Shen et al., 2005; Zormpa et al., 2025; Liu et al., 2022; Sorensen and Shen, 2002). With the potential for AGWs to cause an inflow deceleration, a torque controller was implemented so the turbine always operated at the optimal Tip Speed Ratio (TSR) of 9.5. This optimal TSR value, which correlated to the maximum power output, was found from preliminary simulations which covered a full TSR sweep for the turbine.

Table 2. The main AL parameters chosen for the simulation.

No of Blade Points	No of Sampling Points	Sampling distance r_s	ε	Time Step (s)	Smearing Kernel
50	16	$1.1 \cdot 3 \cdot \varepsilon$	$2\Delta_{cell}$	0.195	Spherical Gaussian

In AL model simulations, the common recommendation is to set the time step so the turbine blade tip travels only one cell per iteration, resulting in a more stringent constraint than implied by the Courant-Friedrichs-Lewy (CFL) condition. The line averaging velocity sampling method was used in this work, following the demonstration of Zormpa et al. (2025) that it allows larger time steps to be taken than other sampling methods with negligible impact on accuracy. Consequently, the time step was set so the blade tip travelled at most three cells, which is still considerably more restrictive than a standard CFL limit would require.

2.6 Simulation Suite

A suite of simulations were run as described in Table 3, chosen to allow for the evaluation of gravity wave impacts compared to other factors such as the Coriolis force and turbulence. In all cases the same numerical schemes and general OpenFOAM setup was used, however, the solver was varied to account for the lack of temperature modelling in wave-free cases and the need for a pressure-driven precursor in the turbulent cases.

Table 3. The key parameters of the simulated cases.

Case	Inflow	Inflow Profile	Precursor	Coriolis Force	Thermal Profile	AGW
1	Turbulent	Sheared	Yes	Yes	CNBL	Yes
2	Turbulent	Sheared	Yes	No	Neutral	No
3	Turbulent	Sheared	Yes	Yes	Neutral	No
4	Laminar	Uniform	No	No	CNBL	Yes
5	Laminar	Uniform	No	No	Neutral	No

https://doi.org/10.5194/wes-2026-208
Preprint. Discussion started: 5 November 2026
© Author(s) 2026. CC BY 4.0 License.



eawe european academy of wind energy
Open Access WIND ENERGY SCIENCE DISCUSSIONS

The precursor was run for 90000 s to reach a quasi-steady flow. The successor was then run for 5000 s before data was taken over the following 3000 s. For the successor this was equivalent to the flow at hub height having 1.75 flows through of the domain before data was taken and the data being taken over on average 300 revolutions of the wind turbine. These spin-up times are in line with those in the literature (Allaerts and Meyers, 2017; Lanzilao and Meyers, 2024).

Whilst the above setup and precursor run times were used for the cases expected to produce AGWs (Case 1, Case 4), in Cases 2, 3, and 5 there were no AGWs to be resolved. So in the turbulent wave-free cases (2 and 3) four modifications for computational efficiency were made. First, similar to farm simulations under neutral boundary layers in the literature, the domain size was limited to 1 km in height (Strickland and Stevens, 2022; Calaf et al., 2010). Second, the distance of the turbine from the inlet was reduced to 10 turbine diameters, which was still sufficient to ensure no interaction between the turbine and inlet. Third, the precursor was run for only 45,000 s, as the quasi-steady state was achieved in the neutral boundary layer simulations much faster. Fourth, the successor was run for only 3000 s before data was taken, as time for wave propagation did not have to be accounted for. The overall reduced computational cost, consequently, meant that in Cases 2 and 3 the precursor simulation was run concurrently as shown in Fig. 6, with the precursor being the first section of the overall domain.

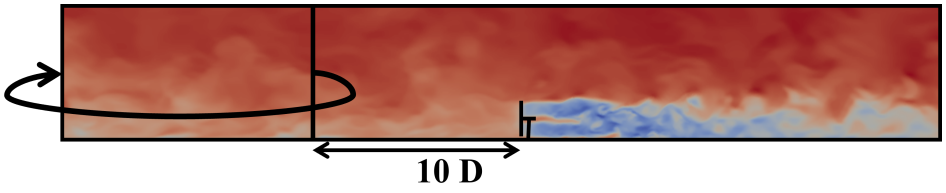


Figure 6. An illustration of the simulation domain for turbulent cases without AGWs. The overall domain is not to scale.

For the majority of the paper, the main case presented will be the turbulent AGW case (Case 1) with a comparison being primarily made to the turbulent wave-free case (Case 2).

3 Results

3.1 Wake Recovery

For Case 1 the time averaged velocity profiles of the geostrophic layer, presented in Fig. 7, demonstrate that the turbine triggered a wave which propagated in both the vertical and horizontal velocity components. A trapped wave is also evident in the temperature field perturbations, travelling horizontally along the inversion layer. The trapped wave temperature perturbation spacing is consistent with the velocity perturbations of the internal waves, confirming that both are driven by a buoyancy mechanism and so can be classified as AGWs. This result is in agreement with the observation of Lanzilao and Meyers (2024) who also noted the development of a trapped wave in their LES wind farm simulations as a result of temperature oscillations in the inversion layer. By tracking the position of temperature isotherms the height of the inversion layer centre is visualised in Fig. 7(d). The centre of the inversion layer is displaced compared to the inflow altitude (400 m) and oscillates in-line with the wave fields, confirming that it is a vertical flow displacement which initiates these AGWs.

https://doi.org/10.5194/wes-2026-208
Preprint. Discussion started: 5 November 2026
© Author(s) 2026. CC BY 4.0 License.

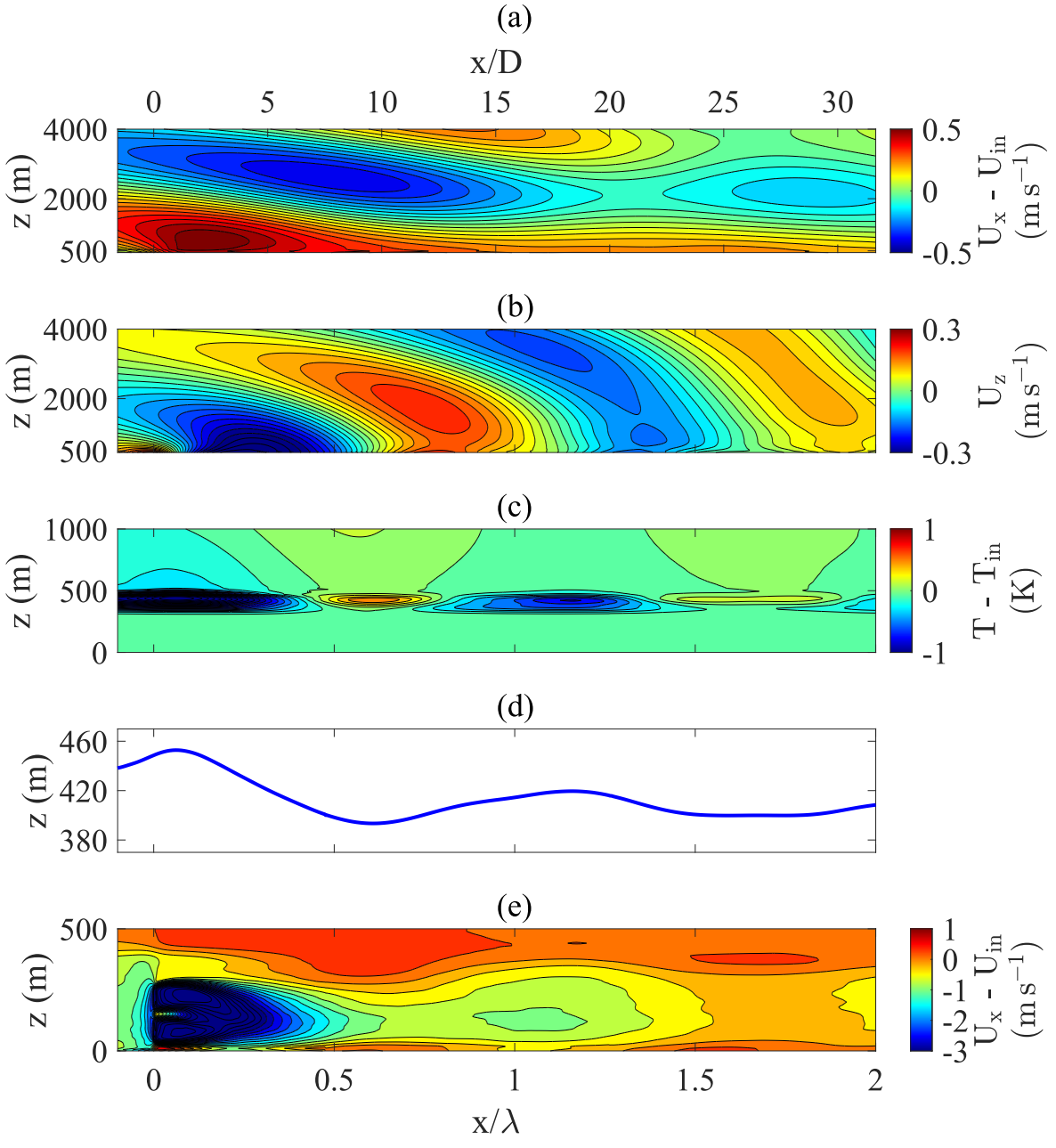


Figure 7. Vertical streamwise planes of the time averaged flow field for Case 1, taken at the centre of the domain and showing the (a) vertical and (b) streamwise velocity in the geostrophic layer, (c) the temperature in the region around the inversion layer and (e) the streamwise velocity for the turbine wake region. To better visualise the perturbation caused by the turbine, in most cases the background flow field ($[\,]_{in}$) has been subtracted. Additionally, in panel (d) the position of the inversion layer centre with streamwise distance is plotted. The x axis datum is taken about the turbine position and the axis is non-dimensionalised on the bottom axes by the predicted AGW's wavelength and on the top axes by the turbine diameter (D).

https://doi.org/10.5194/wes-2026-208
Preprint. Discussion started: 5 November 2026
© Author(s) 2026. CC BY 4.0 License.



eawe european academy of wind energy
Open Access WIND ENERGY SCIENCE DISCUSSIONS

The effect of these waves on the wind turbine wake can be seen when Case 1 is compared to Case 2, an equivalent wave-free simulation, in Fig. 8. In Case 1 the vertical wake width varies sinusoidally with streamwise distance instead of growing consistently as in Case 2. This alteration to wake shape is also apparent in the trajectory of the blade induced vortex structures (see Appendix A). Additionally, the wake recovery in Case 2 is monotonic whilst in Case 1 it is oscillatory, with peaks in the wake velocity in line with the troughs in the AGW field and vice versa for troughs in the wake. At the AGW troughs there are also pockets of accelerated flow outside the wake in Case 1 (dashed boxes in Fig. 8). Whilst in both Cases 1 and 2 accelerated bypass flow is observed above the turbine wake, the pockets of accelerated flow in Case 1 are enhanced compared to bypass acceleration in Case 2 and occur inline with the wave troughs, so are attributable to the AGW. Finally, in Case 1 there is a deceleration upstream of the rotor which, unlike in Case 2, is not just local to the turbine. This has been seen in the literature for farms with AGWs and is often referred to as a wave-induced farm or global blockage effect (Wu and Porté-Agel, 2017; Lanzilao and Meyers, 2024). This effect is attributed to the upstream propagation of the AGW in the literature and as it is only apparent in the simulation with an AGW, these results would be consistent with this explanation. As no farm is simulated in this work, this effect shall be referred to as the AGW-induced flow deceleration.

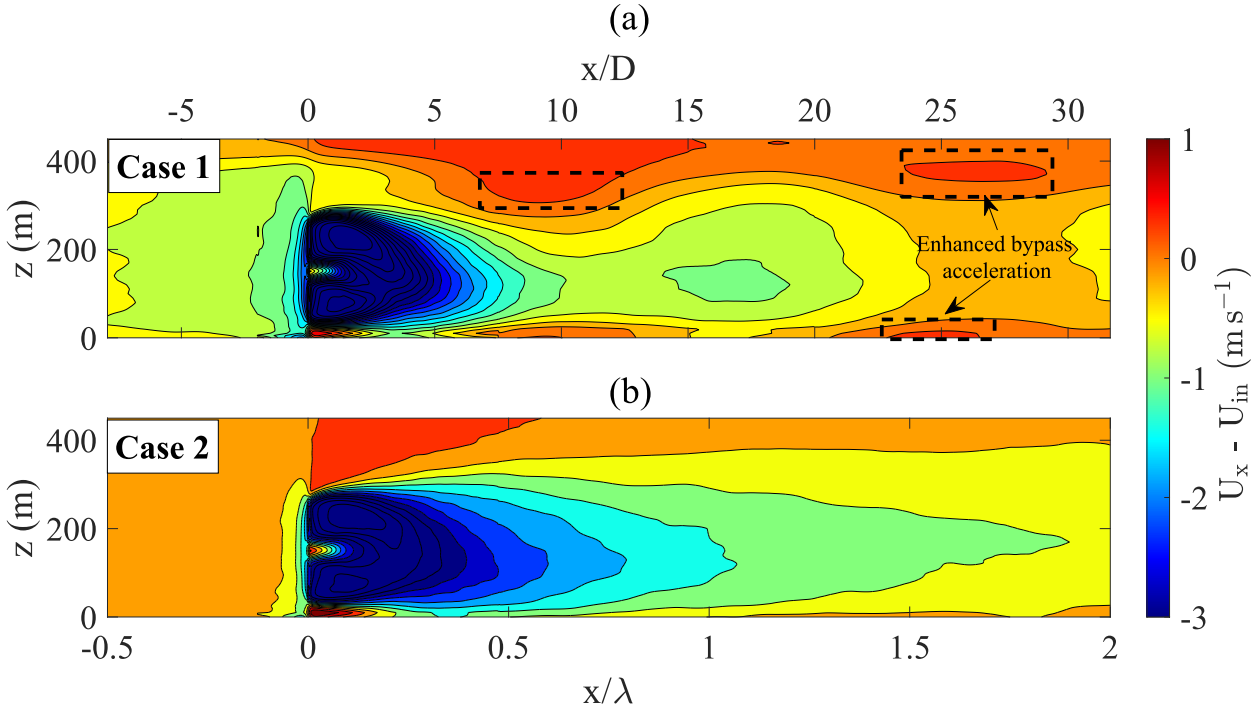
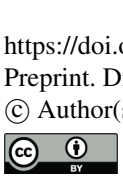


Figure 8. Vertical planes of the time-averaged turbine wake profiles for (a) Case 1 which contains gravity waves and for (b) Case 2 which does not. Dashed boxes are added in (a) to highlight regions of enhanced bypass accelerated flow. The velocity is shown relative to the unperturbed flow. The top x axis is normalised by the turbine diameter and the bottom axis by the theoretical gravity wavelength with the datum taken as the turbine position.

https://doi.org/10.5194/wes-2026-208
Preprint. Discussion started: 5 November 2026
© Author(s) 2026. CC BY 4.0 License.



eawe european academy of wind energy
Open Access WIND ENERGY SCIENCE DISCUSSIONS

A horizontal slice at hub height of the turbine wake for both Cases 1 and 2 are shown in Fig. 9. These again demonstrate that the AGWs cause a non-local deceleration in front of the turbine as seen in Fig. 7. The deceleration resulted in a reduction of 26 % in the mean power and 18 % in the mean thrust for Case 1 when compared to Case 2. The AGW-induced deceleration is particularly large here due to the simulation setup whereby only the central turbine in a farm was modelled, so it does not capture any lateral diversion of flow expected around a farm (Allaerts and Meyers, 2017; Lanzilao and Meyers, 2022; Wu and Porté-Agel, 2017). Whilst in some farm cases the low inversion layer itself can explain the reduced farm power production as a result of lower turbulent entrainment (Abkar and Porté-Agel, 2013), this is unlikely here as the upper atmosphere only becomes a key source of energy deep into farms (Stevens and Meneveau, 2017).

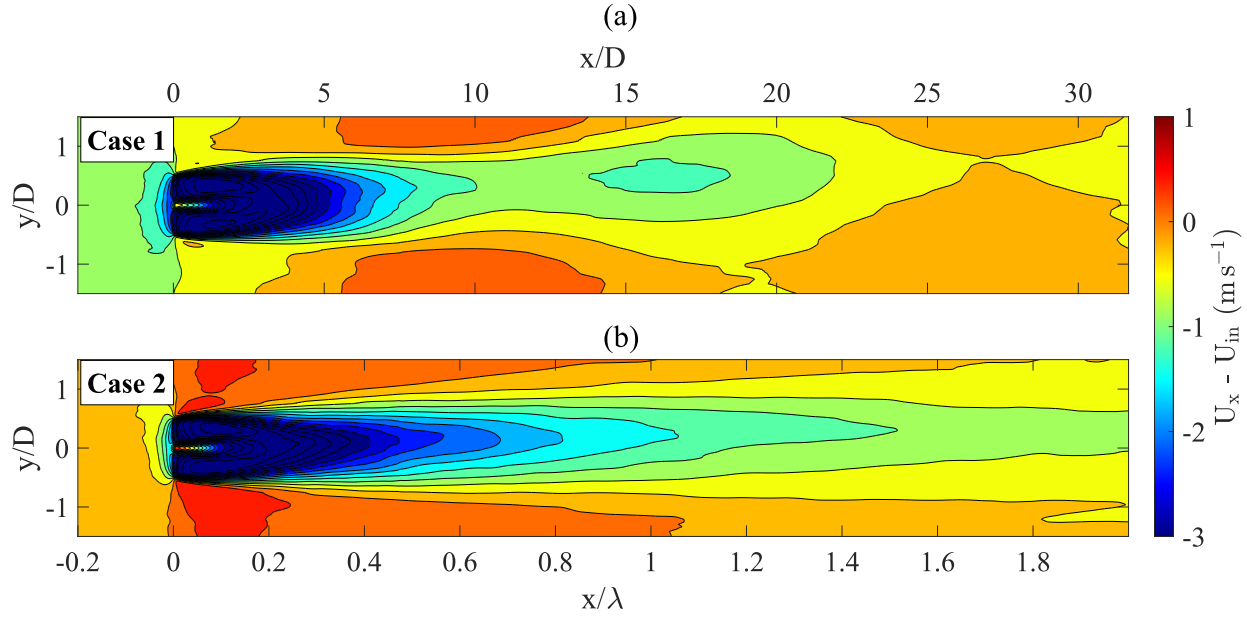


Figure 9. Horizontal planes of the wind turbine wake time-averaged velocity deficits taken in the streamwise direction for Cases (a) 1 and (b) 2. The x and y axes are taken about the turbine position. The top x axis is normalised by the turbine diameter and bottom x axis is normalised by the predicted gravity wavelength. The y axes in both panels are normalised by the turbine diameter.

Furthermore, in Fig. 9, regions of acceleration and deceleration are observed in the wake for Case 1. These regions coincide with the troughs and peaks of the AGWs, consistent with those seen in the vertical profile. The horizontal wake profile in the AGW scenario also shows a variation in width, with a narrowing in line with the first wave trough downstream of the turbine. This, together with the observed wake shape changes in Fig. 7 and A1, demonstrates that AGWs modified the wake in both lateral and streamwise directions. The overall wake shape, consequently, is similar to a cylinder with a diameter sinusoidally varying with streamwise distance. The accelerations in flow seen inline with the wave troughs can be explained by considering the vertical flow confinement from the inversion layer. At a wave trough the inversion layer is reduced in height and thus to conserve mass flux the flow must accelerate. Through this reasoning the inversion layer can be thought to act as a rigid lid, a

https://doi.org/10.5194/wes-2026-208
Preprint. Discussion started: 5 November 2026
© Author(s) 2026. CC BY 4.0 License.



eawe european academy of wind energy
Open Access WIND ENERGY SCIENCE DISCUSSIONS

concept which was used by Stipa et al. (2024a) to simulate AGWs effects by deforming the top boundary in an LES simulation instead of resolving the waves themselves.

Finally in Fig. 9, for Case 1 there is a streamwise horizontal displacement of the wake when compared to case 2. The centre of mass approach given by Eq. 9 was used to evaluate the wake centreline displacement:

$$y_{centre} = \frac{\sum y \cdot \left(1 - \frac{U_x}{U_{up}}\right)^3}{\sum \left(1 - \frac{U_x}{U_{up}}\right)^3} \tag{9}$$

where y_{centre} is the wake centre position as a function of streamwise distance, $U(x)$ is the velocity in the wake and U_{up} is the velocity taken upstream of the rotor as to account for the AGW-induced deceleration.

Comparing Cases 1 to 4 in Fig. 10, Case 1 is the only wake with clear skew with an angle of 1.54°, relative to the turbine hub. Although there is some horizontal displacement in the other cases, this is comparatively small. The direction of this small displacement was found to be a function of the turbine rotation direction, which was impacting the tip vortex and consequently wake breakdown. Whilst the wake skew in Case 1 does indicate the AGWs may the impact the wake skew angle, another key difference in the turbulent AGW case is the inclusion of the Coriolis force and therefore the inflow also having veer.

There is an open discussion in the literature over the extent to which the Coriolis force and veer can impact the wake skew angle. In the farm simulations of Allaerts and Meyers (2017) as well as those of Maas (2023a, b), all of which contained gravity waves, a rotation in the flow was observed in the farm. In all three cases this was mainly attributed to the horizontal imbalance between the predefined driving pressure gradient and the Coriolis force which varies as a function of velocity. Specifically, the deceleration seen in the wake and AGW-induced deceleration effect meant the Coriolis force reduced, resulting in an anticlockwise rotation. This effect was confirmed as a possible explanation for farm wake rotation by van der Laan and Sørensen (2017) by comparing farms with variable and fixed Coriolis forces, however, it was also found to be dependent on how the wind farm was modelled. Their study also demonstrated that, although the wind veer in the inflow can cause a clockwise wake rotation for a single turbine, in neutral conditions wind veer alone is not strong enough to rotate the wake. In our simulations the wind veer varied over the rotor diameter by 4–5° and the Coriolis force was scaled with velocity.

https://doi.org/10.5194/wes-2026-208
Preprint. Discussion started: 5 November 2026
© Author(s) 2026. CC BY 4.0 License.

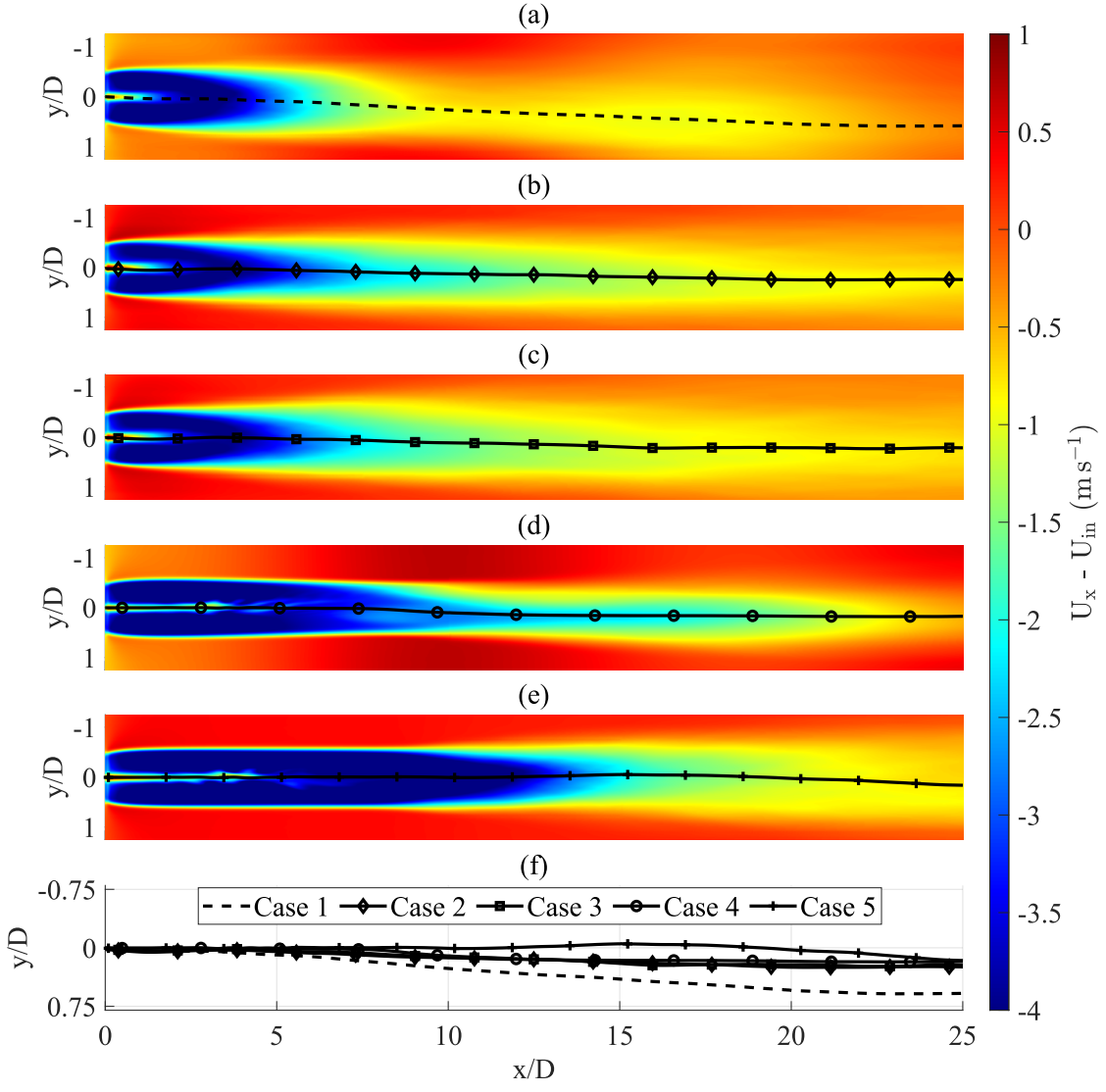


Figure 10. Time-averaged streamwise velocity on horizontal planes at hub height for cases (a) 1, (b) 2, (c) 3, (d) 4 and (e) 5. In addition the centreline for each wake is overlaid onto the plane, with all the cases centrelines plotted together in (f). The x and y axis datum is taken as the turbine centre and the axes are non-dimensionalised by the rotor diameter (D).

Taking horizontal planes for Case 1 at 100 m above and below hub height in Fig. 11 (a-d) shows that the wake skew angle varies with height. For Case 3, a variation of skew angle with height was also seen (Fig. 11 (e-h)), however, the skew angles are rotated compared to those of Case 1. The variation in wake skew with height confirms that the wake skew is being primarily driven by the Coriolis force and its induced wind veer. Additionally, the difference between Case 1 and 3 indicates the AGWs are modifying this skew by creating or enhancing an imbalance between the Coriolis force and driving pressure gradient. The

https://doi.org/10.5194/wes-2026-208
Preprint. Discussion started: 5 November 2026
© Author(s) 2026. CC BY 4.0 License.

imbalance is caused by the speed reduction as a result of AGW-induced deceleration and the wake deficit. At hub height, where the inflow is aligned with the rotor, the wake skew is considerable in Case 1 compared to Case 3 so the AGW-induced deceleration is concluded to be acting as a compounding mechanism in causing the imbalance. Nonetheless, the AGWs are not the driving factor behind the wake skew, as they do not amplify, damp or initiate it. Instead the AGWs just cause an angular shift in the wake skew with height.

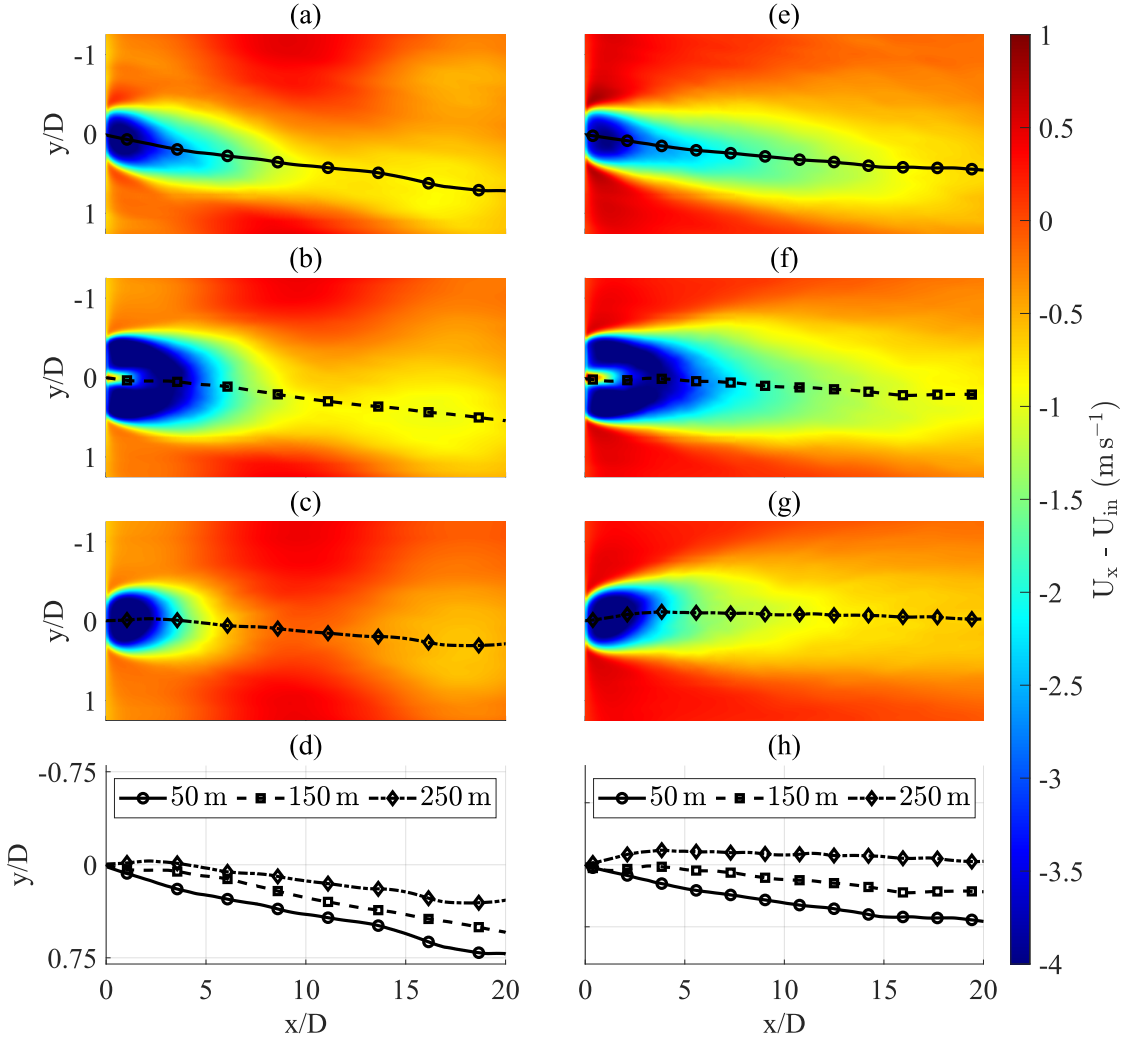


Figure 11. Horizontal planes of the velocity deficit field for Case 1 (a-c) and Case 3 (e-g) in the streamwise direction at heights of (a,e) 50 m, (b,f) 150 m and (c,g) 250 m. The wake centrelines are overlaid onto the plots and plotted together in (d) and (h) for Case 1 and 3 respectively. The axis datum is the turbine position and the axes are non-dimensionalised by the rotor diameter.

Overall the variations between the cases demonstrate that AGWs can impact turbine-scale flows, altering the wake shape, wake recovery and turbine power production. This impact on the turbine scale flow field means the wake shadowing effect be-

https://doi.org/10.5194/wes-2026-208
Preprint. Discussion started: 5 November 2026
© Author(s) 2026. CC BY 4.0 License.



eawe european academy of wind energy
Open Access WIND ENERGY SCIENCE DISCUSSIONS

tween turbines will be altered under AGW conditions and may or may not be favourable depending on the AGW wavelength. Additionally, the change to the flow field through the AGW-induced deceleration reduced the blade loading (Appendix B). However, the waves had no significant impact on the spatial or temporal distribution of the blade loading. Finally, the simulations confirm it is possible to trigger AGWs using a simplified setup with only one turbine row. This suggests that a large farm may not be required to trigger these waves; under favourable thermal conditions, such as a low inversion layer, even a single turbine may be sufficient to trigger AGWs.

3.2 Wake Recovery Mechanisms

The turbine wake velocity profiles presented in Section 3.1 demonstrate the AGWs have an impact on the recovery and dynamics of the wake. Figure 12 compares the streamwise evolution of the wake-averaged velocity for Cases 1 and 2. The wake-average was found by averaging the velocity deficit over a circular area of radius 130 m centred on the wake centreline at hub height. The presence of the AGW in Case 1 results in a non-monotonic recovery of flow speed in the wake, unlike the AGW-free case. Consequently, evaluating wake recovery solely based on wake velocity thresholds may not adequately capture the full dynamics of the turbine wake.

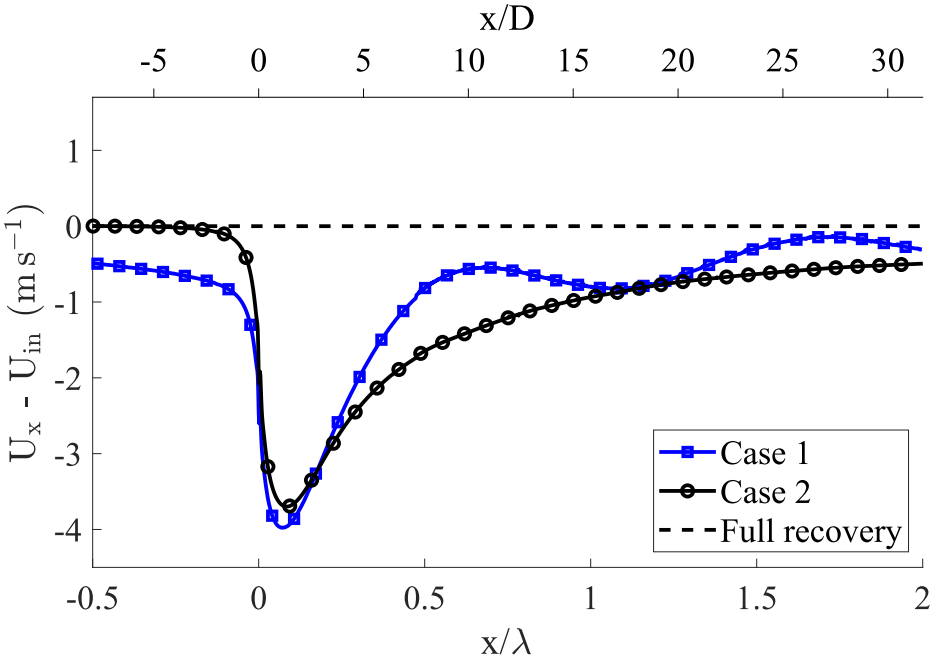


Figure 12. Streamwise evolution of the wake-averaged velocity relative to the inflow for Cases 1 and 2 in the streamwise direction. A dashed line is added to indicate the level at which full flow speed recovery would be achieved. The x axis is taken about the turbine positions and normalised by both the predicted AGW wavelength and turbine diameter.

https://doi.org/10.5194/wes-2026-208
Preprint. Discussion started: 5 November 2026
© Author(s) 2026. CC BY 4.0 License.



eawe european academy of wind energy
Open Access WIND ENERGY SCIENCE DISCUSSIONS

The spatial oscillation in the time averaged velocity along the wake indicates the mean flow component was impacted by the AGWs. Thus, a mean kinetic energy budget analysis was carried out for the wake. Each term in the momentum equation was multiplied by the instantaneous velocity, time averaged and then integrated over the wake length. The control volume for the integration had a width equal to the domain, a height of 300 m and a length increasing with 0.5 D intervals starting from the rotor. The control volume height was chosen to fully capture the turbine wake whilst being lower than the inversion layer even when displaced by AGWs.

The resulting mean kinetic energy budgets are shown in Fig. 13 for both Case 1 and 2. To assist interpretation of the budget, the terms of the momentum equation (Eq. 2) are identified as:

$$\underbrace{\frac{\partial \tilde{u}_i}{\partial t}}_{\text{Temporal derivative}} + \underbrace{\frac{\partial}{\partial x_j}\left(\tilde{u}_j \tilde{u}_i\right)}_{\text{Convection}} = \underbrace{-2\varepsilon_{i3k}\Omega_3 \tilde{u}_k}_{\text{Coriolis}} \underbrace{-\frac{\partial p'}{\partial x_i}}_{\text{Local Pressure}} \underbrace{-\frac{\partial}{\partial x_i}\left\langle \frac{p_0(x,y)}{\rho_0} \right\rangle}_{\text{Background pressure}} \underbrace{-\frac{\partial}{\partial x_j}\left(\tau_{ij}^D\right)}_{\text{Turbulence}} \underbrace{-g_3 z \frac{\partial}{\partial x_i}\left(\frac{\rho_b}{\rho_0}\right)}_{\text{Buoyancy}} + \underbrace{F_i}_{\text{Damping /Turbine Forcing}} \tag{10}$$

Terms for the damping region and the turbine were excluded as they only act on regions outside of the wake. The background pressure gradient was not calculated in Case 2, however, as it is constant throughout the domain, this does not impact the interpretation of the results. In Case 1, shown in Fig. 13(a), the local pressure term and convective term dominate the energy budget oscillating between maxima and minima in line with the gravity wave. Whilst in Case 2, shown by Fig. 13(b), the convective and local pressure terms become of similar magnitude to the other terms which all have a monotonic relationship with the wake distance. Therefore, it can be concluded that AGWs have a significant impact on the mean flow which manifests as a spatially varying momentum exchange between the pressure field and convection terms.

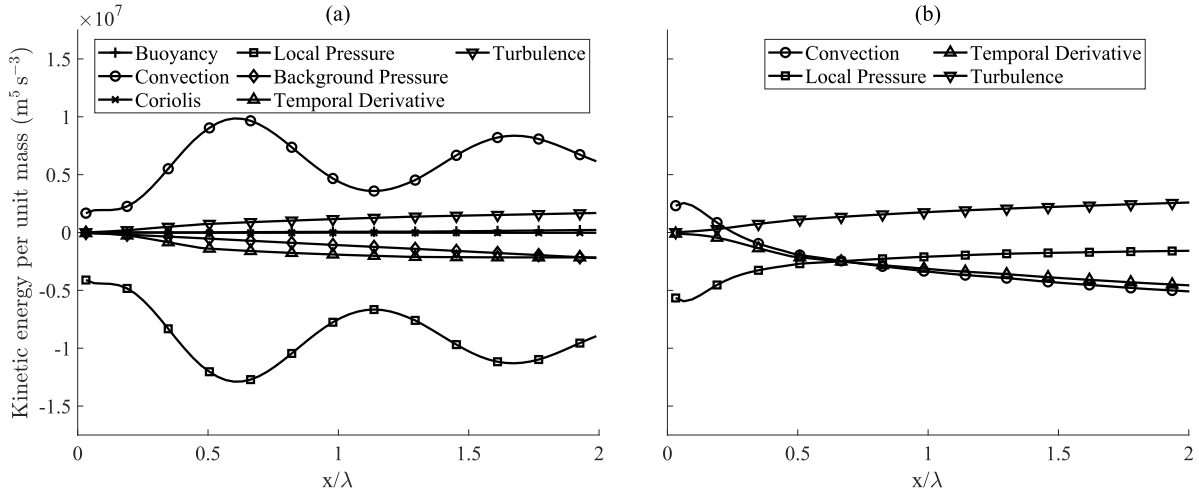


Figure 13. The key mean kinetic energy budget terms integrated over the wake for (a) Case 1 and (b) Case 2. The x axis datum is the rotor position with the first point from a control volume with streamwise length of half a rotor diameter. The x axis is non-dimensionalised by the predicted AGW wavelength (λ).

https://doi.org/10.5194/wes-2026-208
Preprint. Discussion started: 5 November 2026
© Author(s) 2026. CC BY 4.0 License.



eawe european academy of wind energy
Open Access WIND ENERGY SCIENCE DISCUSSIONS

The AGWS may also impact the turbulent component of the wake. The sum of the resolved and modelled components of the TKE was integrated over a control volume which was the same as that for the mean kinetic energy budget. The total TKE for Cases 1 and 2 is plotted in Fig. 14. Case 2 has a higher total TKE in the wake and so would normally be expected to recover faster.

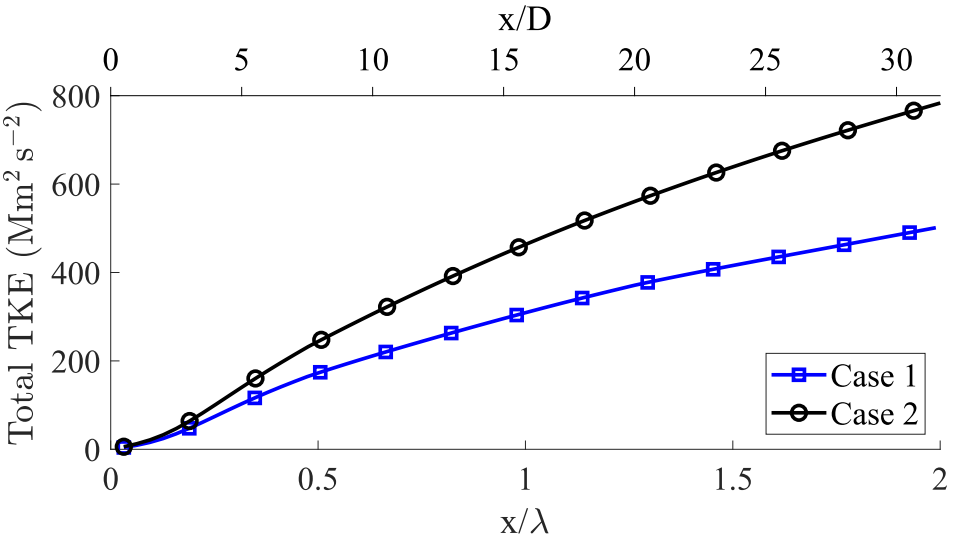


Figure 14. The total Turbulent Kinetic Energy (TKE) integrated over the wake for Cases 1 and 2. The x axis datum is the rotor position and the x axis is non-dimensionalised by the predicted AGW wavelength (λ) and the turbine diameter (D).

To assess if the difference in TKE was caused by the AGWs, an analysis was undertaken of the TKE production and transport in the wake. The TKE budget evaluation followed that of Wu and Porté-Agel (2012) focusing on the three key terms that they identified for wakes under atmospheric flows. First, the production term TKE_P given by,

$$TKE_P = \sum_{i=1}^{3}\sum_{j=1}^{3} -\left(\overline{\tilde{u}_i'\tilde{u}_j'} + \overline{\tau_{ij}^{sgs}}\right)\frac{\partial \overline{\tilde{u}_i}}{\partial x_j} \tag{11}$$

where $'$ indicates a fluctuating component. Second, the advection term TKE_A is given by

$$TKE_A = \sum_{j=1}^{3} -\overline{\tilde{u}_j}\frac{\partial k}{\partial x_j}, \tag{12}$$

where

$$k = \sum_{i=1}^{3}\left(\overline{\tilde{u}_i'\tilde{u}_i'} + \overline{\tau_{ii}^{sgs}}\right). \tag{13}$$

Third, the transport term TKE_T is given by

$$TKE_T = -\frac{1}{2}\sum_{i=1}^{3}\sum_{j=1}^{3}\frac{\partial \overline{\tilde{u}_j'\tilde{u}_j'\tilde{u}_i'}}{\partial x_i} \tag{14}$$

https://doi.org/10.5194/wes-2026-208
Preprint. Discussion started: 5 November 2026
© Author(s) 2026. CC BY 4.0 License.



eawe european academy of wind energy
Open Access WIND ENERGY SCIENCE DISCUSSIONS

To account for potential differences in TKE caused by the Coriolis force, Case 3 is also compared (Abkar and Porté-Agel, 2016). The three TKE components in the vertical streamwise plane are shown for Cases 1, 2 and 3 in Fig. 15, 16 and 17 respectively. In all three components, Cases 2 and 3 have a stronger intensity in the wake compared to Case 1. The differences in the intensity of the components between the cases is consistent with the differences in flow speed and thus turbine thrust, with only Case 1 experiencing wave-induced flow deceleration. In Case 1 the advection and transport in the wake is confined by the inversion layer, whilst in Case 2 and 3 it freely extends vertically with streamwise distance. In all three cases the wake breakdown occurs around 2 to 3 D as indicated by the increase in TKE production consistent with the tip vortex breakdown. The TKE is then transported through the wake over 3 to 5 D behind the rotor in all three cases. Therefore, when comparing Case 1 to Cases 2 and 3 there are no significant streamwise variations in any of the TKE terms as a result of the AGWs, with changes being on the order of magnitude of those from just adding the Coriolis force (Case 2 vs Case 3).

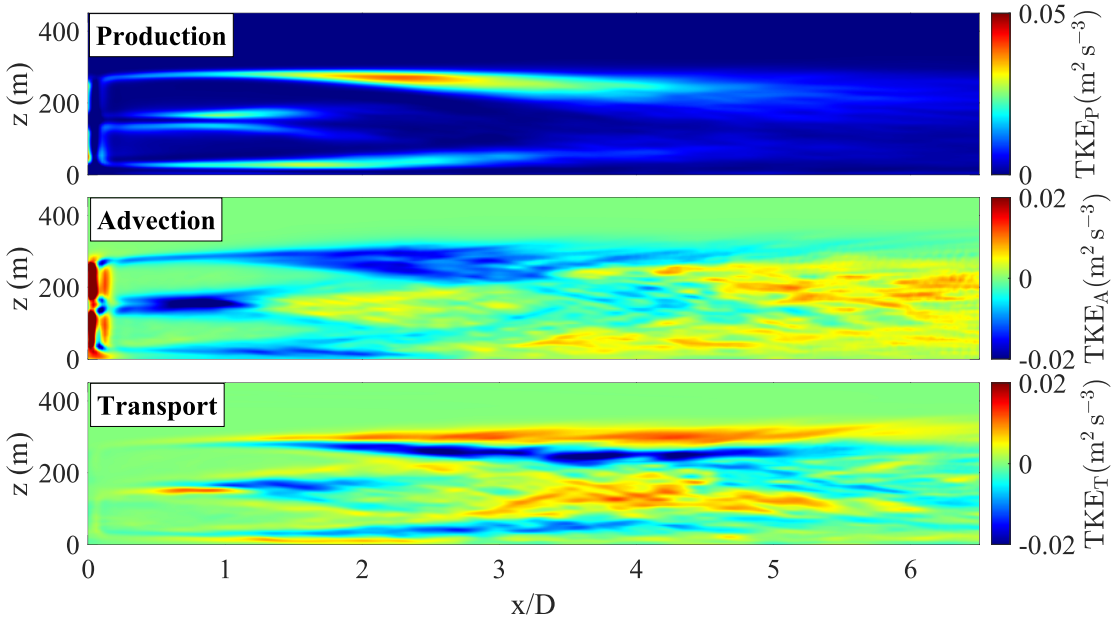


Figure 15. The TKE production, advection and transport over the turbine wake for Case 1. The x axis datum is taken at the rotor position and non-dimensionalised by the rotor diameter.

https://doi.org/10.5194/wes-2026-208
Preprint. Discussion started: 5 November 2026
© Author(s) 2026. CC BY 4.0 License.

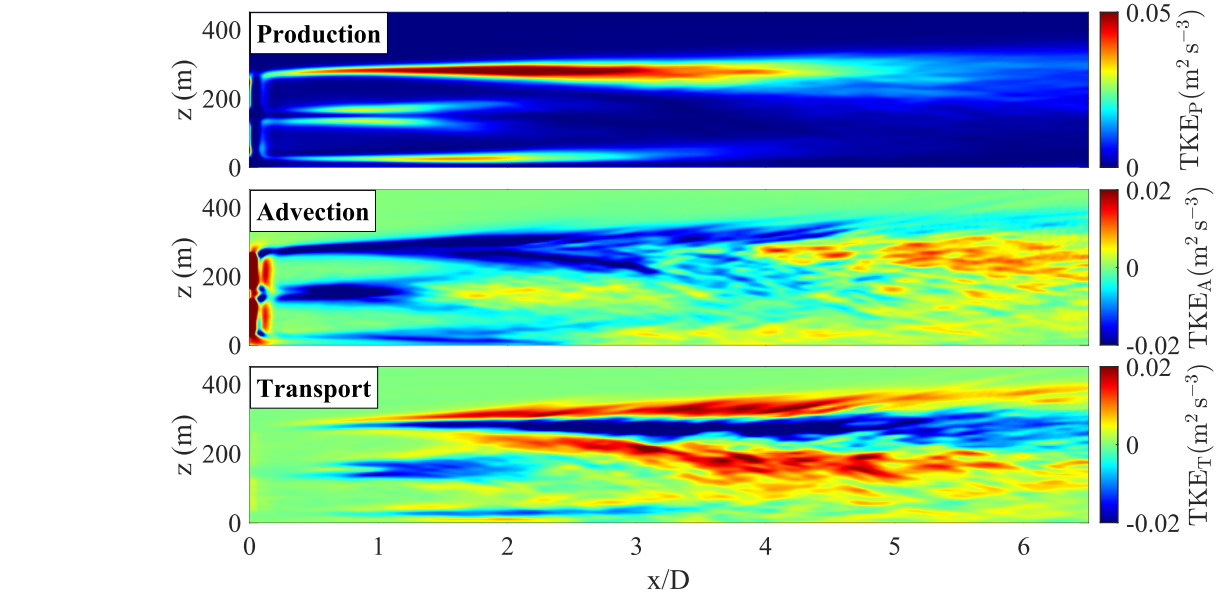


Figure 16. The TKE production, advection and transport over the turbine wake for Case 2. The x axis datum is taken at the rotor position and non-dimensionalised by the rotor diameter.

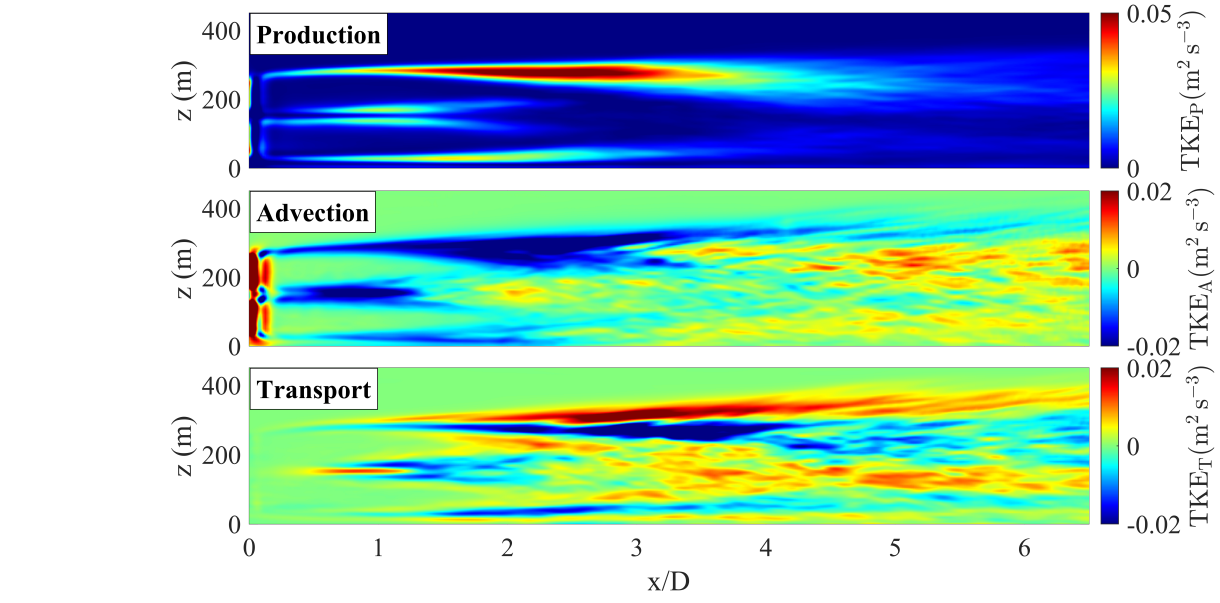


Figure 17. The TKE production, advection and transport over the turbine wake for Case 3. The x axis datum is taken at the rotor position and non-dimensionalised by the rotor diameter.

https://doi.org/10.5194/wes-2026-208
Preprint. Discussion started: 5 November 2026
© Author(s) 2026. CC BY 4.0 License.



eawe european academy of wind energy
Open Access WIND ENERGY SCIENCE DISCUSSIONS

In all three cases two terms dominate in the TKE production:

$$\mathrm{II} = -\left(\overline{\tilde{u}'\tilde{v}'} + \overline{\tau_{12}^{sgs}}\right)\frac{\partial\overline{\tilde{u}}}{\partial y} \tag{15}$$

and

$$\mathrm{III} = -\left(\overline{\tilde{u}'\tilde{w}'} + \overline{\tau_{13}^{sgs}}\right)\frac{\partial\overline{\tilde{u}}}{\partial z} \tag{16}$$

consistent with the finding of Wu and Porté-Agel (2012). Cross-stream slices close to the production terms peak, 3 D behind the rotor, are shown in Fig. 18. Cases 1 and 3 show asymmetric profiles of TKE production terms II and III, due to the Coriolis force, unlike Case 2 without the Coriolis force.

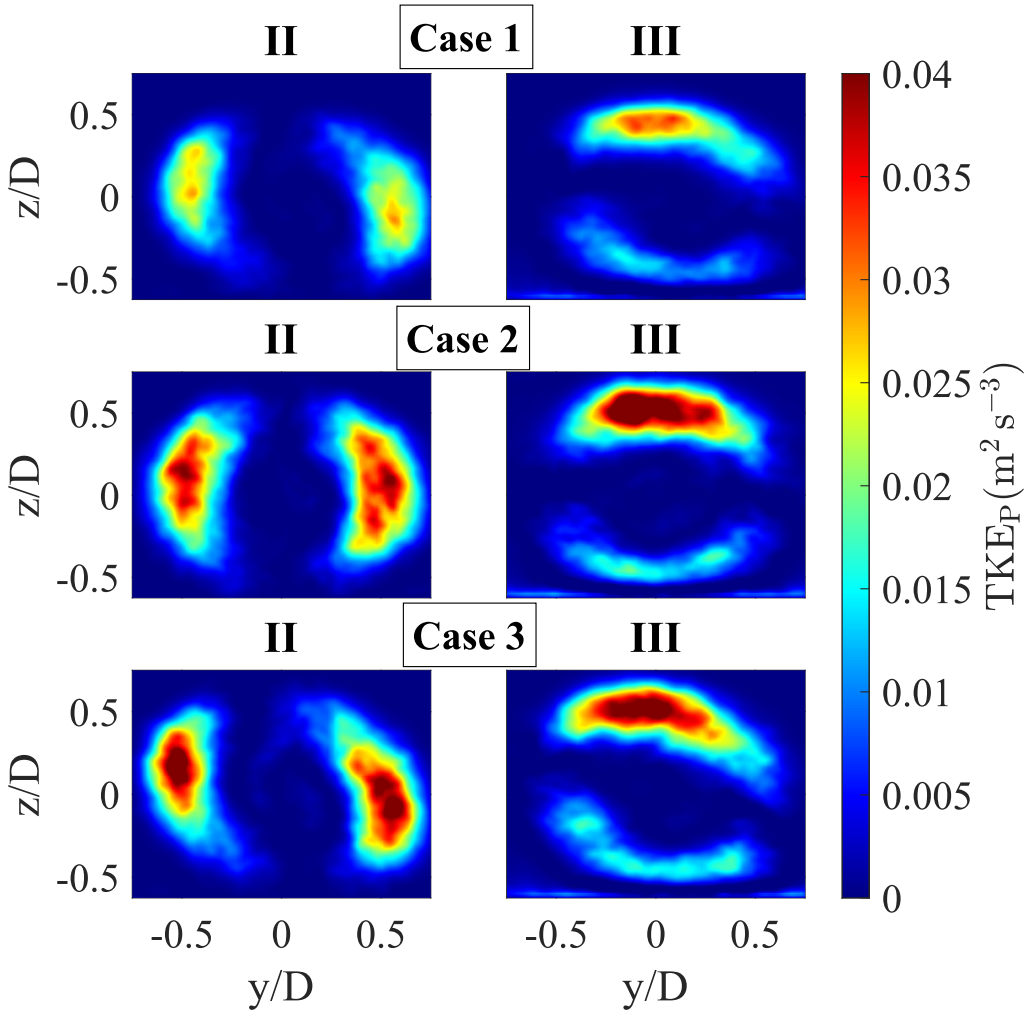


Figure 18. A vertical plane at $x = 3\,D$ for Cases 1 to 3, showing the II and III components of TKE production. The axes are taken relative to the turbine position and non-dimensionalised by the turbine diameter.

https://doi.org/10.5194/wes-2026-208
Preprint. Discussion started: 5 November 2026
© Author(s) 2026. CC BY 4.0 License.



eawe european academy of wind energy
Open Access WIND ENERGY SCIENCE DISCUSSIONS

The analysis of the TKE and mean energy budgets indicates that AGWs primarily interact with the mean flow and do not significantly impact the fluctuating components. Therefore, the AGWs could be considered a purely inviscid mechanism acting independently of the turbulence of the flow. Furthermore, the conventional approach for assessing wake recovery based solely on the mean velocity deficit may not be sufficient in cases where gravity waves significantly influence the mean flow dynamics. Instead, alternative metrics such as the turbulence intensity could be used for measuring recovery, as shown in Fig. 19. As turbulence intensity is based on the fluctuating components of the flow, the streamwise evolution of this metric is independent of the gravity wave effects. Therefore, with this alternative metric the streamwise position of full wake recovery can be assessed using a threshold based on the inflow conditions.

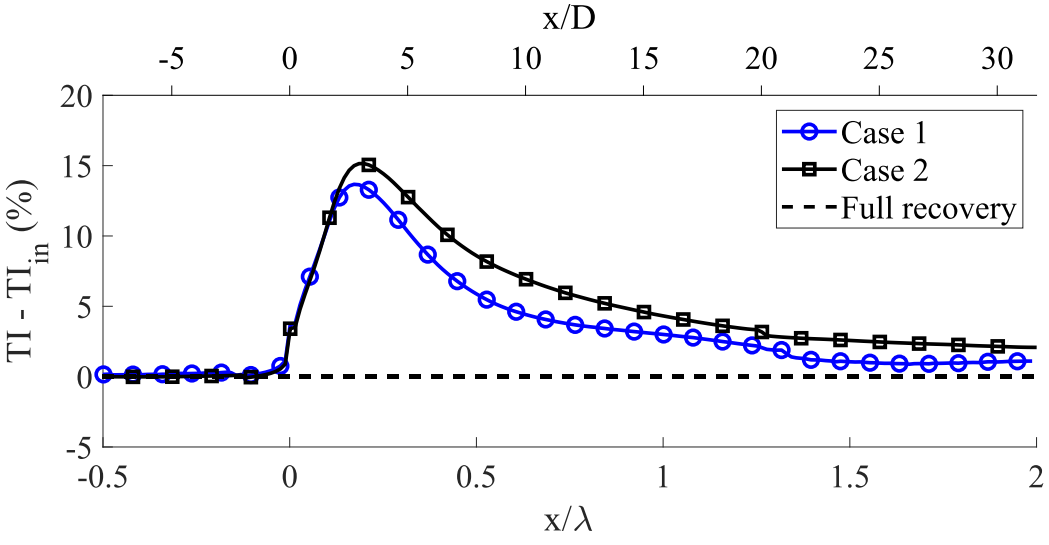


Figure 19. Streamwise evolution of the wake-averaged Turbulence Intensity (TI) for Cases 1 and 2. The TI is relative to the background with a dashed line added to the plot to indicate full return to the background TI state (TI_{in}). The x axis is taken about the rotor position and non-dimensionalised by both the rotor diameter and predicted AGW wavelength.

3.3 Impact of Lateral Spacing

As shown in previous sections, flow confinement is a key mechanism through which gravity waves affect rotor and wake flows. In this section, the domain width is varied, emulating different lateral spacings between neighbouring rotors. Only results for cases with AGWs and turbulent inflows are presented.

Figure 20 compares the triggered gravity waves in the case of 3 diameter (3 D) and 6 diameter (6 D) lateral spacings. A reduction in the internal wave strength is evident when the lateral spacing is increased, however, there is no change to the spatial distribution of the waves between the spacing cases.

https://doi.org/10.5194/wes-2026-208
Preprint. Discussion started: 5 November 2026
© Author(s) 2026. CC BY 4.0 License.

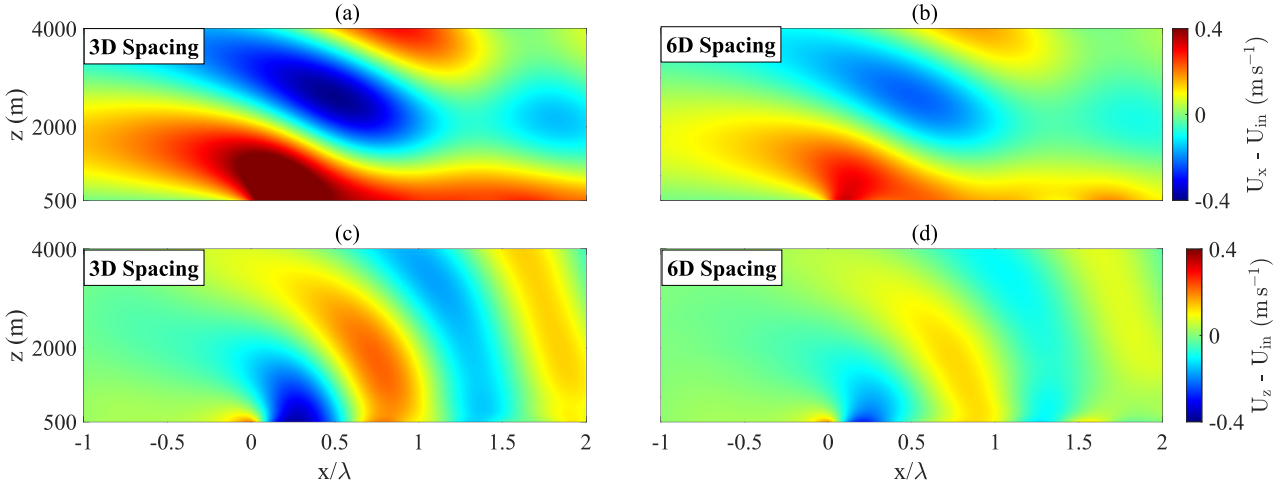


Figure 20. Streamwise vertical planes of the flow field focussing on the AGWs in the geostrophic layer above the turbine. In panels (a), (b) the streamwise velocity relative to the background (U_x-$U_{x,in}$) is plotted and in (c), (d) the vertical velocity relative to the background (U_z-$U_{z,in}$). The left panels plot the flow field for a lateral spacing of three turbine diameters, and the right for six diameters. The x axis is taken about the turbine position and non-dimensionalised by the predicted AGW wavelength.

Comparing the temperature profiles between the 3 D and 6 D spacing cases in Fig. 21, shows a decrease in the strength of the perturbation to the inversion layer. This correlates with the reduction seen in the vertical velocity profiles, demonstrating that it is a weakening of the buoyancy mechanism causing a change in the wave strength. This change is caused by the wider spacing allowing more lateral bypass flow and consequently there is less vertical bypass flow, resulting in less deflection of the inversion layer, shown by the temperature perturbation above the turbine in the 3 D case being stronger than that in the 6 D case.

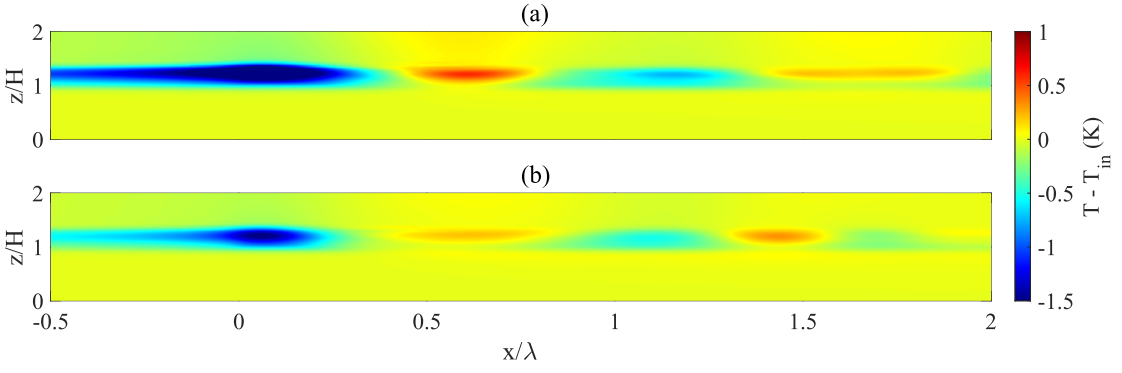


Figure 21. Vertical streamwise planes focussed on the inversion layer, showing the temperature field relative to the background field (T-T_{in}) for a turbine lateral spacing of (a) 3 D and (b) 6 D. The z axis is non-dimensionalised by the inversion layer height and the x axis by the AGW wavelength.

https://doi.org/10.5194/wes-2026-208
Preprint. Discussion started: 5 November 2026
© Author(s) 2026. CC BY 4.0 License.

A comparison between the horizontal wake profiles is presented in Fig. 22, showing a reduction in the magnitude of the wake evolution characteristics attributed to gravity waves in the 6 D case compared to the 3 D case. In the 6 D case there is some reduction in wake veer, however, this is relatively small, demonstrating that AGWs are not the driving factor of this feature. In the 6 D case there is also a decrease in the wake narrowing consistent with a lessening of the acceleration at the wave trough. Finally, there is a greater upstream deceleration in the 3 D case compared to the 6 D case.

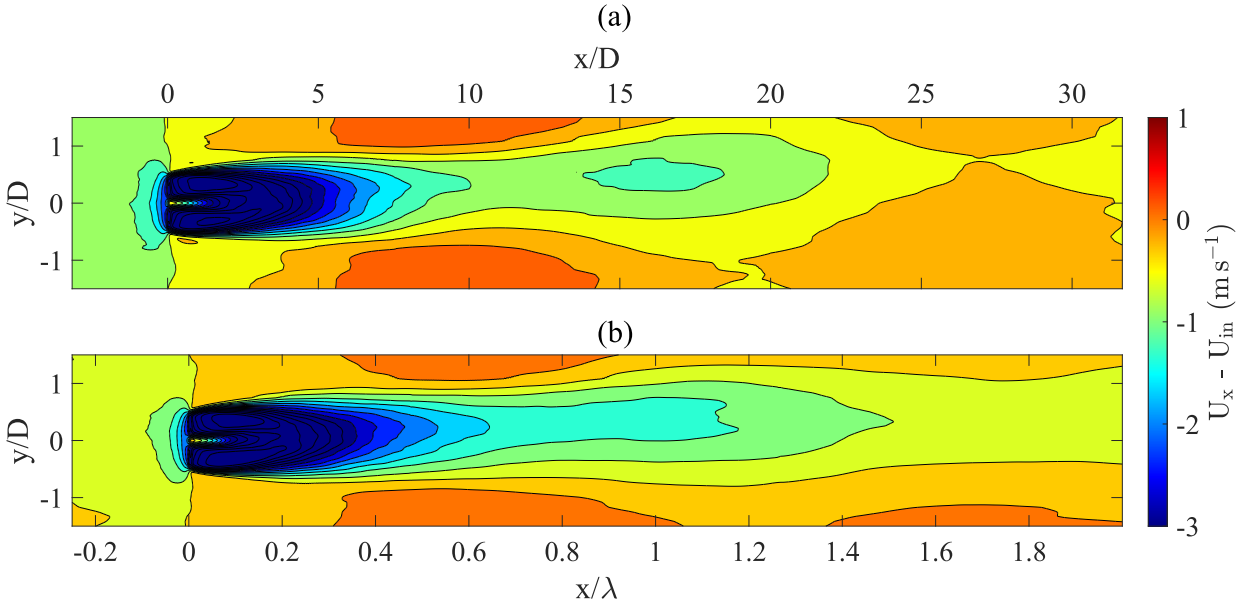


Figure 22. Streamwise horizontal planes of the turbine wakes for (a) a case with 3 D lateral turbine spacing and (b) 6 D lateral spacing. Both axes are taken relative to the turbine position. The y axis is non-dimensionalised by the turbine diameter. The x axis is non-dimensionalised by in (a) the turbine diameter and in (b) the predicted AGW wavelength.

These observations are further corroborated in the comparison of the vertical profiles of the wake velocity deficit in Fig. 23 for spacings of 3 D, 4.5 D, 6 D and 7.5 D. The acceleration pockets diminish, the upstream flow deceleration reduces, the wake width is closer to monotonic in growth and the oscillation in wake velocity lessens as the lateral spacing increases. Furthermore, in Fig. 23 the case with a rotor spacing of 7.5 D has a velocity deficit of 0.5 to 1 $\mathrm{m\,s^{-1}}$ at 1.5 to 2 λ downstream of the rotor whilst the velocity deficit of the 3 D spacing case is closer to 0 to 0.5 $\mathrm{m\,s^{-1}}$. The reduced deficit in the tighter spacing case is caused by the lower turbine thrust as a result of increased AGW-induced deceleration. This difference in the downstream velocity deficit means that lateral spacing could have a considerable impact on the wake shadowing effect on downstream turbines.

https://doi.org/10.5194/wes-2026-208
Preprint. Discussion started: 5 November 2026
© Author(s) 2026. CC BY 4.0 License.

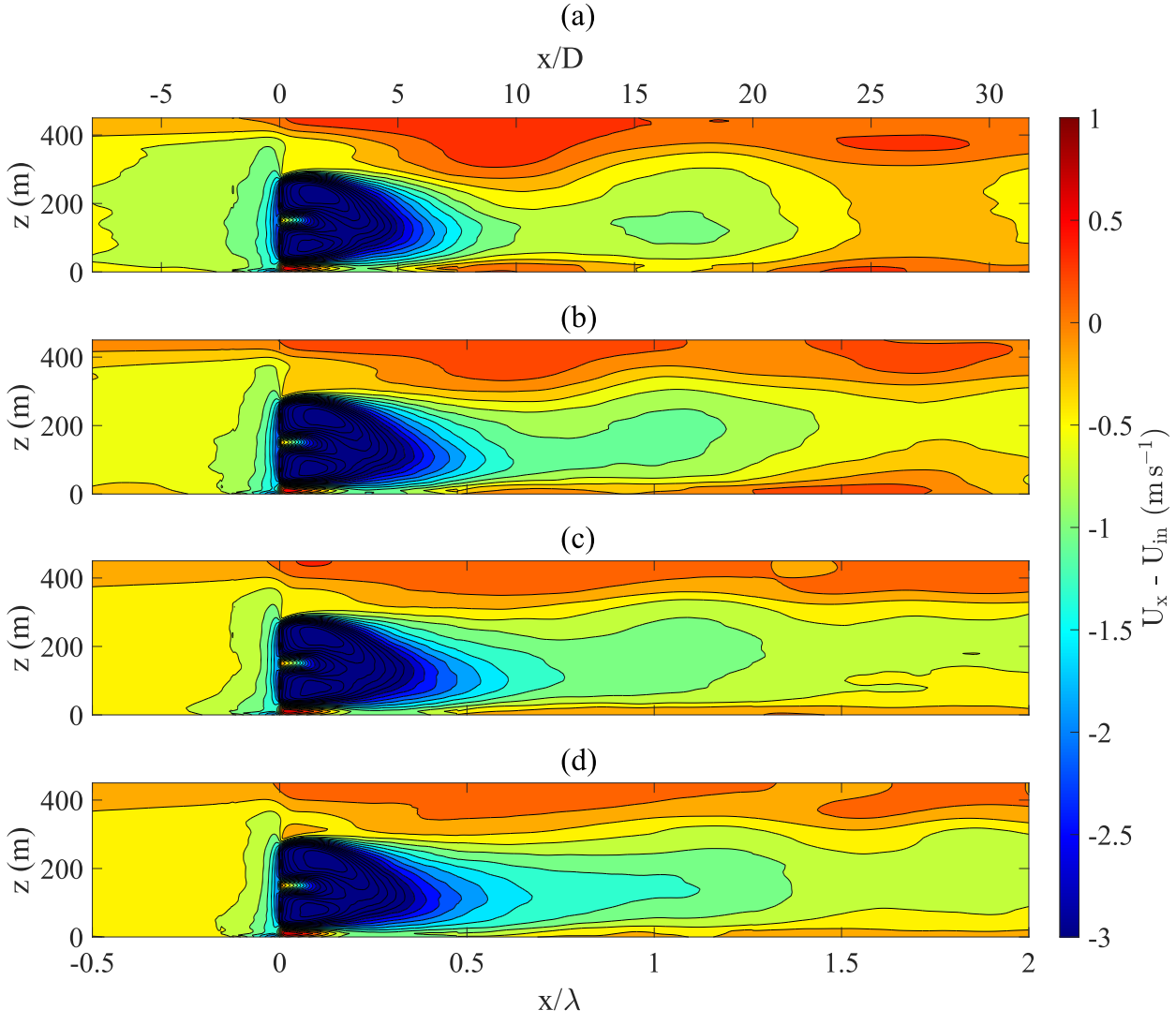


Figure 23. Streamwise vertical planes of the turbine wakes for cases with (a) 3 D, (b) 4.5 D, (c) 6 D and (d) 7.5 D lateral spacing. The x axis is taken relative to the turbine position and non-dimensionalised by both the predicted AGW wavelength and the turbine diameter.

By visualising the change to the vertical profile of the horizontally-averaged streamwise velocity U_x at 5 D upstream, outside the rotor induction region, in Fig. 24(a) the AGW-induced deceleration is evident in both uniform and turbulent inflow cases. Within the vertical extent of the rotor, the velocity deficit is similar in both inflow cases, consistent with AGWs behaving as a largely inviscid mechanism. Furthermore, as the lateral spacing increases linearly the AGW-induced deceleration decreases non-linearly (Fig. 24(b)). The deceleration reduction attenuates with spacing, implying a minimum AGW-induced deceleration and thus AGW that could develop.

https://doi.org/10.5194/wes-2026-208
Preprint. Discussion started: 5 November 2026
© Author(s) 2026. CC BY 4.0 License.

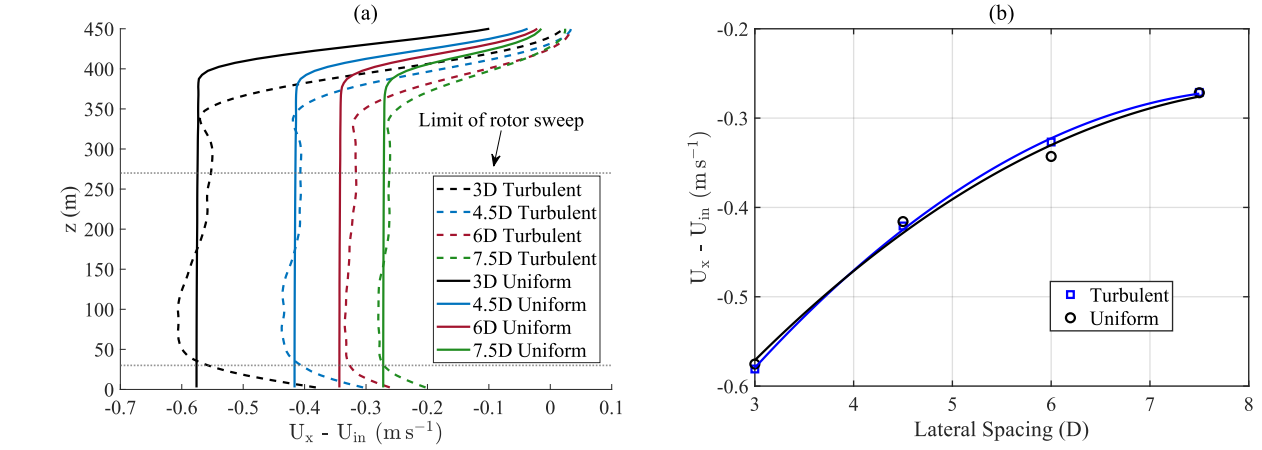


Figure 24. Plots of the horizontally averaged velocity relative to the inflow at 5 D upstream of the rotor for different turbine lateral spacings, with (a) showing the deficit profile and (b) the deficit averaged over the rotors vertical extent. The results for both cases with turbulent and uniform inflow are plotted. The horizontal dashed lines in (a) indicate the the vertical extent of the rotor swept area. The curve fitted to the data in panel (b) is a 2nd order polynomial.

The change to the trapped wave field from the variation in lateral spacing is also captured in the displacement extent of the inversion layer. By tracking the vertical position of temperature isotherms in the streamwise direction and comparing this to the position at the inflow, the displacement of the inversion layer along the domain centre is plotted in Fig. 25. The shape of the inversion displacement, its magnitude and phase are relatively consistent between the cases with turbulent and uniform inflows. This suggests that the wave field, and thus the displacement mechanism by which the waves are initiated, is independent of the turbulence of the ambient flow.

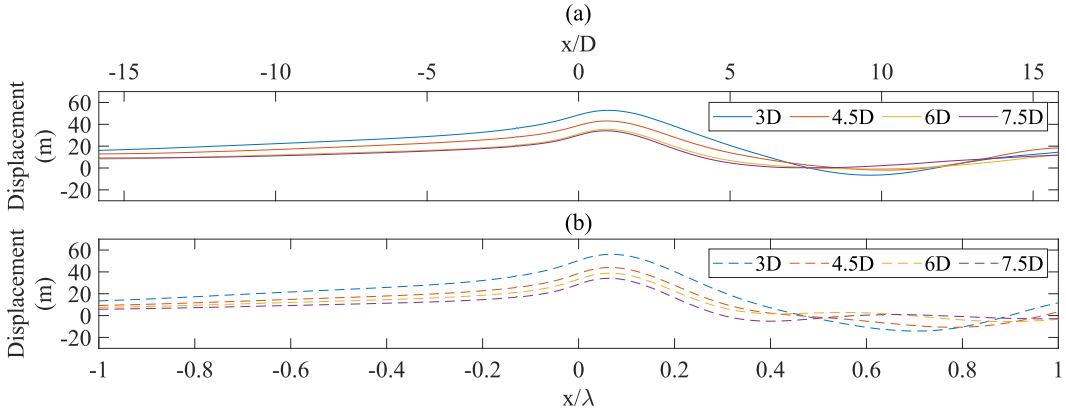


Figure 25. Vertical displacement of the inversion layer along the centre of the domain in the streamwise direction. Cases with a turbulent inflow are shown in (a) and a uniform inflow in (b) for cases with varying lateral spacing. The x axis is taken relative to the turbine position and non-dimensionalised by both the predicted AGW wavelength and the turbine diameter.

https://doi.org/10.5194/wes-2026-208
Preprint. Discussion started: 5 November 2026
© Author(s) 2026. CC BY 4.0 License.



eawe european academy of wind energy
Open Access WIND ENERGY SCIENCE DISCUSSIONS

Both turbulent and uniform inflow cases also show a consistent trend in the reduction of inversion layer displacement with increased spacing. The attenuation of the trapped AGW amplitude is quantified by comparing the maximum perturbation to the inversion layer in Fig. 26(a) for different spacings. Figure 26(a) shows that the maximum perturbation decreases with increasing lateral spacing but this happens at a decreasing rate of change. The convergence of the result on a peak change of $\sim$60 % of the initial value at 7.5 D spacing suggests that for large turbines, even when operating in isolation, an AGW may develop if the inversion layer is low enough.

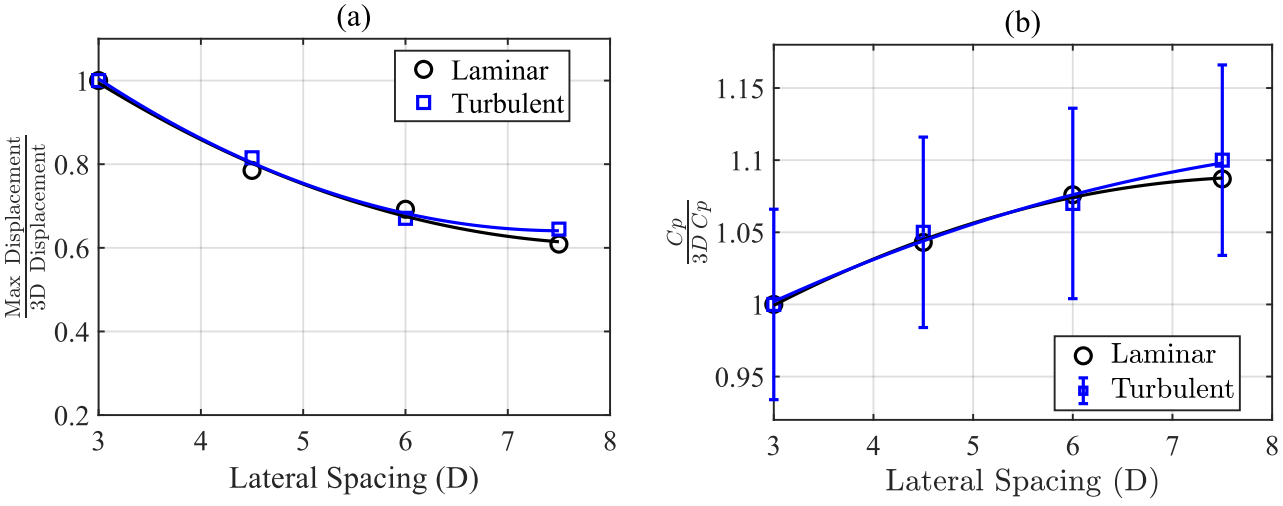


Figure 26. Changes to (a) the maximum inversion layer displacement and (b) power coefficient for different lateral turbine spacings. In both (a) and (b) the y axes have been non-dimensionalised by the 3 D spacing case. Error bars representing one standard deviation in the power are included in (b). The curves fitted to the data are 2nd order polynomials in both panels.

A change in the power production consistent with that of the inversion layer perturbation was also observed. The power coefficient of the turbine for varying spacing is given in Fig. 26(b) and was calculated based on the undisturbed flow field. At 7.5 D spacing the power produced is around 10 % higher than at 3 D spacing. Whilst this is a significant increase in power, it is much lower than the wave-free scenarios, with Cases 2 and 3 producing 36 % and 32 % more power than the 3 D case respectively. Differences in the undisturbed flow between the cases accounts for only a relatively small proportion of this change in power production, as demonstrated by the difference between Cases 2 and 3. Therefore, the substantial discrepancy between the AGW and wave-free cases is indicative of how influential AGWs are on power production. The significance of the AGW impact is further evidenced by considering that at a tighter turbine lateral spacing the resulting greater geometric blockage ratio normally would be expected to result in an increased power production. However, these results show the opposite trend with power gain despite a greater lateral spacing, thus, demonstrating the major influence gravity waves have on turbine power production. Consequently, this supports AGW atmospheric scenarios and their frequency being accounted for in future farm planning for both layout and location.

https://doi.org/10.5194/wes-2026-208
Preprint. Discussion started: 5 November 2026
© Author(s) 2026. CC BY 4.0 License.



Finally, both the uniform and turbulent inflow cases demonstrate similar trends despite differences in the inflow conditions. Whilst some of this similarity comes from normalisation of the results to account for a logarithmic or uniform inflow profile, it also supports the hypothesis that the AGWs and their effects on rotors are independent of the turbulence of the flow. Therefore, whilst the AGWs that develop may depend on the farm design and operation parameters, they may be independent of the flow characteristics inside the farm itself.

4 Discussion and Conclusions

In this work, AGWs have been shown to have a significant impact on wind turbine scale flows. The rate of wake recovery, the wake shape and the wake skew were all altered by the AGWs. These modifications to the wake dynamics and their magnitude are important to capture as they could impact the predicted extent of the wake shadowing within wind farms and consequently the performance of downstream turbines. Furthermore, the magnitude of the wake modifications were shown to be a function of the wave strength, which could be altered by varying the lateral turbine spacing. Rafferty and Vogel (2026) demonstrated the AGW strength was strongly correlated to turbine thrust. Thus, the streamwise spacing of potential downstream turbines may also impact the wave strength through a thrust variation from the non-monotonicity in the recovery of the wake of the upstream turbine. As the wake monotonicity, the wave induced deceleration and wake length were all observed in this work to be a function of wave strength, the streamwise positions of turbine rows could create a complex feedback loop. Overall this work suggests both the lateral and streamwise farm spacing are likely to have a crucial role in the extent of the expected AGW influence in wind farms. In addition, these findings indicate the possibility of optimal farm layouts for AGW scenarios. Understanding these scenarios could also be used to explain potential variations seen in the farm power patterns and improve farm control strategies under AGW conditions.

Evaluation of energy budgets in the turbine wake demonstrate that AGWs predominantly interact with the pressure field and convection in the mean flow. Additionally, the consistency of the observed trends between the uniform and turbulent inflow cases suggest the AGW wave generation and their effects are largely independent of the fluctuating component of the flow. Together, these findings indicate that the AGW dynamics are primarily governed by inviscid mechanisms.

The results also suggest there is a scale separation, whereby the AGWs do impact the turbine-scale flows, whilst remaining relatively insensitive to the flow dynamics at that scale. The separation concept is advantageous for modelling, as it means that simplified setups with low fidelity turbine or farm models would suffice for the accurate prediction and assessment of an AGW field, which is consistent with the findings of Rafferty and Vogel (2026). Moreover, the separation suggests that the flow field only needs to be captured at a high resolution within the boundary layer for cases where intra-farm wake interactions and blade loading are being assessed.

One of the key impacts of the AGWs observed was a deceleration upstream of the rotor, below the boundary layer and spanning the width of the domain. In the cases without AGWs, however, there was no appreciable deceleration upstream of the rotor. Therefore, it can be concluded that no global or farm blockage was present in the simulations, consistent with only one turbine being simulated. Similarly, the difference between the cases means the deceleration that was seen must have been

https://doi.org/10.5194/wes-2026-208
Preprint. Discussion started: 5 November 2026
© Author(s) 2026. CC BY 4.0 License.

AGW induced. Consequently, the AGWs are concluded to be a compounding effect to the decelerations seen in the wider wind farm literature and not an enhancement of the farm blockage mechanism.

Whilst the use of an infinite row to simulate the AGWs will have over-emphasised the strength of the AGWs triggered, this work has demonstrated a potential lower computational cost methodology than full farm simulations that is still capable of capturing gravity waves. The amplification of the waves allowed analysis of the role of AGWs in observations such as the wake skew and recovery where other atmospheric factors, such as the Coriolis force and turbulence intensity, play a prominent role. Furthermore, as only one turbine was simulated, this work indicates it may be possible to trigger gravity waves with clusters of turbines rather than just farms. Therefore, understanding the typical atmospheric thermal parameters at a location, such as the inversion layer, will likely be of importance for all scales of installation planning.

Finally, AGWs can be triggered under any positively stratified thermal condition (Nappo, 2012). Therefore, while only a CNBL flow case was simulated in this work, the findings on the underlying physics, sensitivity to parameters and impact to the turbine scale flows, could be of use to a wider range of scenarios. For example it would be worthwhile considering the impact of AGWs for turbines under diurnal cycles or onshore near wave inducing topographical features such as mountain ridges or tree canopies.

Appendix A: Appendix A

The impact of the AGW on the wake shape can be seen through the trajectory of the tip and hub vortices, visualised using the time averaged vorticity of the flow field as shown in Fig. A1. Cases 4 and 5, where the inflow is uniform, are included here because the overall wake structure lasts longer allowing for better visualisation. In both the turbulent and uniform inflow AGW cases the tip vortex is forced downwards whilst in the wave-free case it extends in the horizontal direction. This shape is consistent with the shape of the oscillation in the inversion layer which varies from a peak just after the turbine to a trough at 7 to 8 D downstream of the rotor. This demonstrates that one impact of the inversion layer is to confine the wake.

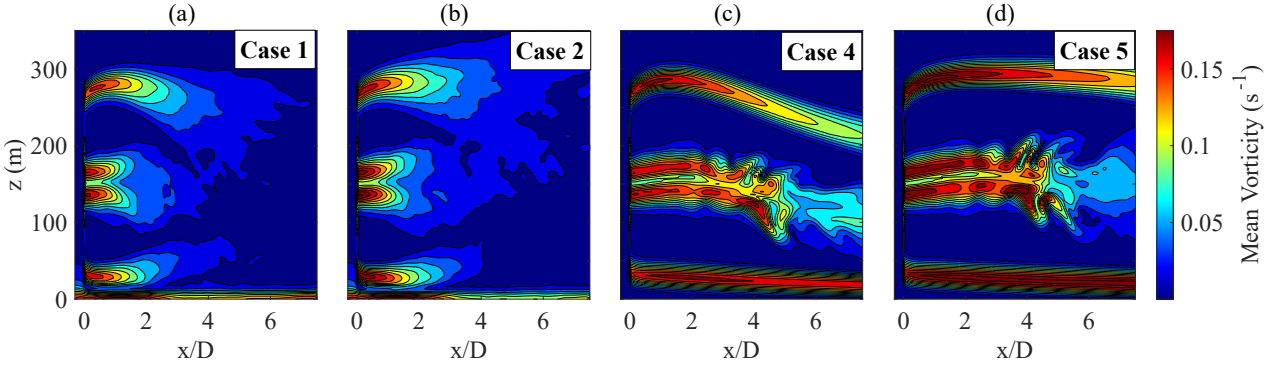


Figure A1. Vertical streamwise planes of the time-averaged vorticity magnitude for Cases (a) 1, (b) 2, (c) 4 and (d) 5. The x axis is taken about the turbine position and non-dimensionalised by the turbine diameter.

https://doi.org/10.5194/wes-2026-208
Preprint. Discussion started: 5 November 2026
© Author(s) 2026. CC BY 4.0 License.



eawe european academy of wind energy
Open Access WIND ENERGY SCIENCE DISCUSSIONS

Appendix B: Appendix B

Blade loads were binned into 5° for calculation of the flapwise and edgewise Root Bending Moments (RBM). Comparing the RBMs of Case 1 to Case 2 in Fig. B1 shows a consistent reduction in the loading, with the mean reducing by ∼19 % and ∼18 % in the edgewise and flapwise RBM respectively. This change is due to the AGW-induced deceleration upstream of the turbine. Figure B1 also shows the blades underwent cyclic loading due to operating in a sheared flow profile. Normalising the root bending moments by the mean loading of the respective cases in Fig. B1, shows no significant difference in the loading pattern between Case 1 and 2 is apparent. This indicates the AGW-induced deceleration in Case 1 is causing primarily a bulk deceleration of the flow in the swept area of the rotor. Whilst there is a small increase in the loading seen in Case 2 compared to 3 this driven by the flatter vertical shear profile caused by the inclusion of the Coriolis force.

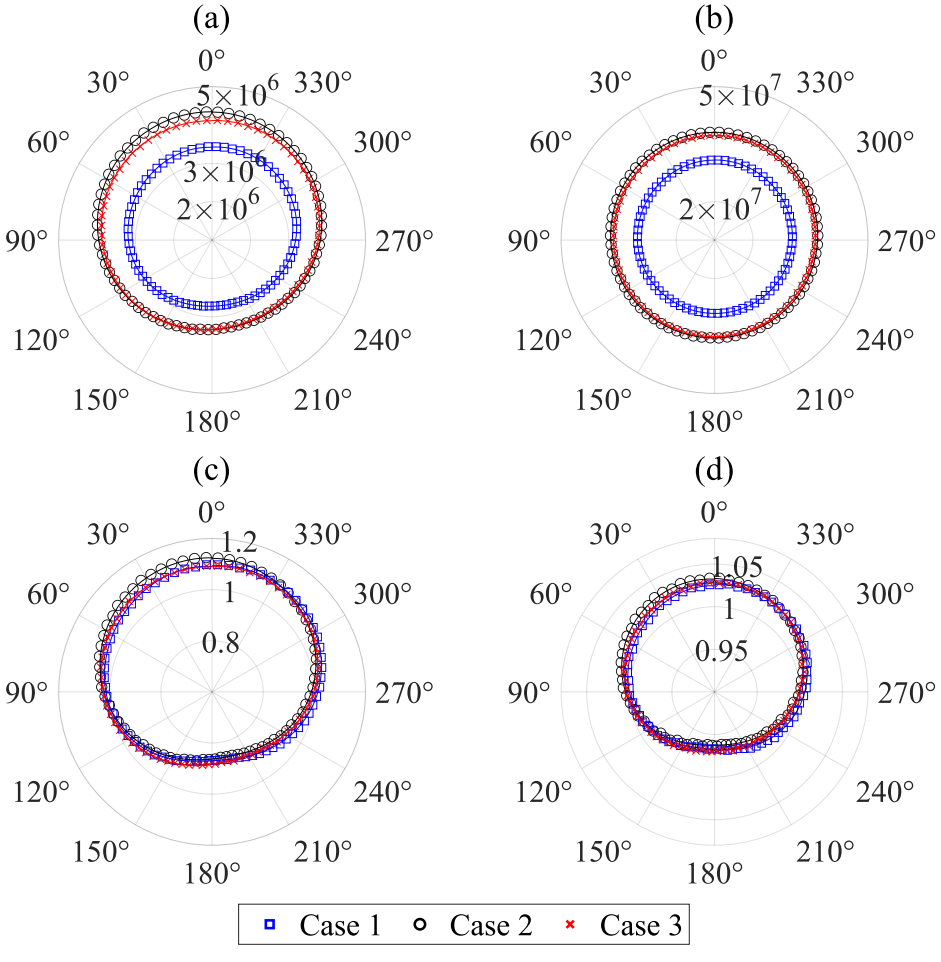


Figure B1. Polar plots for the Root Bending Moments (RBM) of a turbine blade over the 360° sweep for Cases 1 to 3. Plots (a) and (b) are the edgewise and flapwise RBM respectively in N m. Plots (c) and (d) are again the edgewise and flapwise RBM respectively, normalised by the mean value over the whole sweep. In all four panels 0° is when the blade tip is at the highest point.

https://doi.org/10.5194/wes-2026-208
Preprint. Discussion started: 5 November 2026
© Author(s) 2026. CC BY 4.0 License.



eawe european academy of wind energy
Open Access WIND ENERGY SCIENCE DISCUSSIONS

Data availability. The solver used, SOWFA, is publicly available and held in the NLR GitHub repository. The raw simulation dataset is not currently publicly available, but, can be provided by the corresponding author upon reasonable request.

Author contributions. Both authors contributed equally to the conception of the simulations and the discussion of the results. TR ran the simulations, post-processed the results, and wrote the first draft of the paper. The article was internally reviewed and finalised by both authors.

Competing interests. No competing interests are present

Acknowledgements. T.R acknowledges the support of his Margaret Thatcher scholarship and the use of the ARCHER2 UK National Supercomputing Service through the EPSRC Access to HPC project, Wake Aerodynamics of Offshore Wind Turbines. C.R.V. acknowledges the support of UKRI through his Future Leaders Fellowship MR/V02504X/1.

https://doi.org/10.5194/wes-2026-208
Preprint. Discussion started: 5 November 2026
© Author(s) 2026. CC BY 4.0 License.



eawe european academy of wind energy
Open Access WIND ENERGY SCIENCE DISCUSSIONS

References

Abkar, M. and Porté-Agel, F.: The Effect of Free-Atmosphere Stratification on Boundary-Layer Flow and Power Output from Very Large Wind Farms, Energies, 6, 2338–2361, https://doi.org/10.3390/en6052338, 2013.

Abkar, M. and Porté-Agel, F.: Influence of atmospheric stability on wind-turbine wakes: A large-eddy simulation study, Physics of Fluids, 27, 035 104, https://doi.org/10.1063/1.4913695, 2015.

Abkar, M. and Porté-Agel, F.: Influence of the Coriolis force on the structure and evolution of wind turbine wakes, Physical Review Fluids, 1, 063 701, https://doi.org/10.1103/PhysRevFluids.1.063701, 2016.

Allaerts, D. and Meyers, J.: Large eddy simulation of a large wind-turbine array in a conventionally neutral atmospheric boundary layer, Physics of Fluids, 27, 065 108, https://doi.org/10.1063/1.4922339, 2015.

Allaerts, D. and Meyers, J.: Boundary-layer development and gravity waves in conventionally neutral wind farms, Journal of Fluid Mechanics, 814, 95–130, https://doi.org/10.1017/jfm.2017.11, 2017.

Bleeg, J., Purcell, M., Ruisi, R., and Traiger, E.: Wind Farm Blockage and the Consequences of Neglecting Its Impact on Energy Production, Energies, 11, 1609, https://doi.org/10.3390/en11061609, 2018.

Brasseur, J. G. and Wei, T.: Designing large-eddy simulation of the turbulent boundary layer to capture law-of-the-wall scaling, Physics of Fluids, 22, 021 303, https://doi.org/10.1063/1.3319073, 2010.

Calaf, M., Meneveau, C., and Meyers, J.: Large eddy simulation study of fully developed wind-turbine array boundary layers, Physics of Fluids, 22, 015 110, https://doi.org/10.1063/1.3291077, 2010.

Churchfield, M. J., Lee, S., Michalakes, J., and Moriarty, P. J.: A numerical study of the effects of atmospheric and wake turbulence on wind turbine dynamics, Journal of Turbulence, 13, 14, https://doi.org/10.1080/14685248.2012.668191, 2012.

Csanady, G.: Equilibrium theory of the planetary boundary layer with an inversion lid, Boundary-Layer Meteorology, 6, 63–79, https://doi.org/10.1007/BF00232477, 1974.

Dammann, T., Dangi, N., Van Wingerden, J.-W., and Yu, W.: Benchmark Study on Rotor Performance, Wake Dynamics, and Atmospheric Boundary Layers using NREL SOWFA-6 and AMR-WIND, Journal of Physics: Conference Series, 3016, 012 034, https://doi.org/10.1088/1742-6596/3016/1/012034, 2025.

Deardorff, J. W.: Numerical investigation of neutral and unstable planetary boundary layers, Journal of Atmospheric Sciences, 29, 91–115, https://doi.org/10.1175/1520-0469(1972)029<0091:NIONAU>2.0.CO;2, 1972.

Doubrawa, P., Churchfield, M. J., Godvik, M., and Sirnivas, S.: Load response of a floating wind turbine to turbulent atmospheric flow, Applied Energy, 242, 1588–1599, https://doi.org/10.1016/j.apenergy.2019.01.165, 2019.

Fleming, P. A., Gebraad, P. M., Lee, S., van Wingerden, J.-W., Johnson, K., Churchfield, M., Michalakes, J., Spalart, P., and Moriarty, P.: Evaluating techniques for redirecting turbine wakes using SOWFA, Renewable Energy, 70, 211–218, https://doi.org/10.1016/j.renene.2014.02.015, 2014.

Gaertner, E., Rinker, J., Sethuraman, L., Zahle, F., Anderson, B., Barter, G. E., Abbas, N. J., Meng, F., Bortolotti, P., Skrzypinski, W., et al.: IEA Wind TCP Task 37: Definition of the IEA 15-Megawatt Offshore Reference Wind Turbine, Tech. rep., National Renewable Energy Laboratory (NREL), https://doi.org/10.2172/1603478, 2020.

Han, Y., Stoellinger, M. K., Peng, H., Zhang, L., and Liu, W.: Large eddy simulation of atmospheric boundary layer flow over complex terrain in comparison with RANS simulation and on-site measurements under neutral stability condition, Journal of Renewable and Sustainable Energy, 15, 023 301, https://doi.org/10.1063/5.0133585, 2023.

https://doi.org/10.5194/wes-2026-208
Preprint. Discussion started: 5 November 2026
© Author(s) 2026. CC BY 4.0 License.

Jonkman, J., Butterfield, S., Musial, W., and Scott, G.: Definition of a 5-MW Reference Wind Turbine for Offshore System Development, Tech. rep., National Renewable Energy Laboratory (NREL), https://doi.org/10.2172/947422, 2009.

Khan, M. A., Allaerts, D., Watson, S. J., and Churchfield, M. J.: Investigating the relationship between simulation parameters and flow variables in simulating atmospheric gravity waves for wind energy applications, Wind Energy Science, 10, 1167–1185, https://doi.org/10.5194/wes-10-1167-2025, 2025.

Khanna, S. and Brasseur, J. G.: Analysis of Monin–Obukhov similarity from large-eddy simulation, Journal of Fluid Mechanics, 345, 251–286, https://doi.org/10.1017/S0022112097006277, 1997.

Klemp, J. B. and Lilly, D. K.: Numerical Simulation of Hydrostatic Mountain Waves, Journal of Atmospheric Sciences, 35, 78 – 107, https://doi.org/10.1175/1520-0469(1978)035<0078:NSOHMW>2.0.CO;2, 1978.

Lanzilao, L. and Meyers, J.: Effects of self-induced gravity waves on finite wind-farm operations using a large-eddy simulation framework, Journal of Physics: Conference Series, 2265, 022 043, https://doi.org/10.1088/1742-6596/2265/2/022043, 2022.

Lanzilao, L. and Meyers, J.: An improved fringe-region technique for the representation of gravity waves in large eddy simulation with application to wind farms, Boundary-layer meteorology, 186, 567–593, https://doi.org/10.1007/s10546-022-00772-z, 2023.

Lanzilao, L. and Meyers, J.: A parametric large-eddy simulation study of wind-farm blockage and gravity waves in conventionally neutral boundary layers, Journal of Fluid Mechanics, 979, A54, https://doi.org/10.1017/jfm.2023.1088, 2024.

Li, Z., Liu, X., and Yang, X.: Review of turbine parameterization models for large-eddy simulation of wind turbine wakes, Energies, 15, 6533, https://doi.org/10.3390/en15186533, 2022.

Liu, L., Franceschini, L., Oliveira, D. F., Galeazzo, F. C., Carmo, B. S., and Stevens, R. J.: Evaluating the accuracy of the actuator line model against blade element momentum theory in uniform inflow, Wind Energy, 25, 1046–1059, https://doi.org/10.1002/we.2714, 2022.

Maas, O.: From gigawatt to multi-gigawatt wind farms: wake effects, energy budgets and inertial gravity waves investigated by large-eddy simulations, Wind Energy Science, 8, 535–556, https://doi.org/10.5194/wes-8-535-2023, 2023a.

Maas, O.: Large-eddy simulation of a 15 GW wind farm: Flow effects, energy budgets and comparison with wake models, Frontiers in Mechanical Engineering, 9, 1108 180, https://doi.org/10.3389/fmech.2023.1108180, 2023b.

Moeng, C.-H.: A Large-Eddy-Simulation Model for the Study of Planetary Boundary-Layer Turbulence, Journal of Atmospheric Sciences, 41, 2052–2062, https://doi.org/10.1175/1520-0469(1984)041<2052:ALESMF>2.0.CO;2, 1984.

Munters, W., Meneveau, C., and Meyers, J.: Shifted periodic boundary conditions for simulations of wall-bounded turbulent flows, Physics of Fluids, 28, 025 112, https://doi.org/10.1063/1.4941912, 2016.

Nappo, C. J.: An Introduction to Atmospheric Gravity Waves, vol. 102, Academic Press, second edn., ISBN 9780123852236, 2012.

Narasimhan, G., Gayme, D. F., and Meneveau, C.: Analytical model coupling Ekman and surface layer structure in atmospheric boundary layer flows, Boundary-Layer Meteorology, 190, 16, https://doi.org/10.1007/s10546-024-00859-9, 2024.

Ning, X., Krutova, M., and Bakhoday-Paskyabi, M.: Analysis of offshore wind spectra and coherence under neutral stability condition using the two LES models PALM and SOWFA, Journal of Physics: Conference Series, 2018, 012 027, https://doi.org/10.1088/1742-6596/2018/1/012027, 2021.

NLR: SOWFA, Version 6.0, https://github.com/{N}at{L}ab{R}ockies/{SOWFA}-6, (Accessed:March 2024), 2022.

Pope, S.: Turbulent Flows, Cambridge University Press, ISBN 9780521598866, 2000.

Porté-Agel, F., Meneveau, C., and Paralange, M. B.: A scale-dependent dynamic model for large-eddy simulation: application to a neutral atmospheric boundary layer, Journal of Fluid Mechanics, 415, 261–284, https://doi.org/10.1017/S0022112000008776, 2000.

https://doi.org/10.5194/wes-2026-208
Preprint. Discussion started: 5 November 2026
© Author(s) 2026. CC BY 4.0 License.

Porté-Agel, F., Bastankhah, M., and Shamsoddin, S.: Wind-Turbine and Wind-Farm Flows: A Review, Boundary-Layer Meteorology, 174, 1–59, https://doi.org/10.1007/s10546-019-00473-0, 2020.

Rafferty, T. and Vogel, C.: The impact of the turbine model on gravity wave simulations, Journal of Physics: Conference Series, 3224, 032 077, https://doi.org/10.1088/1742-6596/3224/3/032077, 2026.

Revaz, T. and Porté-Agel, F.: Large-eddy simulation of wind turbine flows: A new evaluation of actuator disk models, Energies, 14, 3745, https://doi.org/10.3390/en14133745, 2021.

Sanchez Gomez, M., Lundquist, J. K., Mirocha, J. D., and Arthur, R. S.: Investigating the physical mechanisms that modify wind plant blockage in stable boundary layers, Wind Energy Science, 8, 1049–1069, https://doi.org/10.5194/wes-8-1049-2023, 2023.

Scott, R., Martínez-Tossas, L., Bossuyt, J., Hamilton, N., and Cal, R. B.: Evolution of eddy viscosity in the wake of a wind turbine, Wind Energy Science, 8, 449–463, https://doi.org/10.5194/wes-8-449-2023, 2023.

Shen, W. Z., Mikkelsen, R., Sørensen, J. N., and Bak, C.: Tip loss corrections for wind turbine computations, Wind Energy, 8, 457–475, https://doi.org/10.1002/we.153, 2005.

Smith, R. B.: Gravity wave effects on wind farm efficiency, Wind Energy, 13, 449–458, https://doi.org/10.1002/we.366, 2010.

Sorensen, J. N. and Shen, W. Z.: Numerical modeling of wind turbine wakes, Journal of Fluids Engineering, 124, 393–399, https://doi.org/doi.org/10.1115/1.1471361, 2002.

Spiegel, E. A. and Veronis, G.: On the Boussinesq Approximation for a Compressible Fluid, The Astrophysical Journal, 131, 442, https://doi.org/10.1086/146849, 1960.

Stevens, R. J. and Meneveau, C.: Flow Structure and Turbulence in Wind Farms, Annual Review of Fluid Mechanics, 49, 311–339, https://doi.org/10.1146/annurev-fluid-010816-060206, 2017.

Stipa, S., Ahmed Khan, M., Allaerts, D., and Brinkerhoff, J.: A large-eddy simulation (LES) model for wind-farm-induced atmospheric gravity wave effects inside conventionally neutral boundary layers, Wind Energy Science, 9, 1647–1668, https://doi.org/10.5194/wes-9-1647-2024, 2024a.

Stipa, S., Ajay, A., Allaerts, D., and Brinkerhoff, J.: TOSCA – an open-source, finite-volume, large-eddy simulation (LES) environment for wind farm flows, Wind Energy Science, 9, 297–320, https://doi.org/10.5194/wes-9-297-2024, 2024b.

Strickland, J. M. and Stevens, R. J.: Investigating wind farm blockage in a neutral boundary layer using large-eddy simulations, European Journal of Mechanics - B/Fluids, 95, 303–314, https://doi.org/10.1016/j.euromechflu.2022.05.004, 2022.

Stull, R. B.: Practical Meteorology: an Algebra-based Survey of Atmospheric Science, University of British Columbia, ISBN 978-0-88865-283-6, 2015.

Taylor, J. R. and Sarkar, S.: Internal gravity waves generated by a turbulent bottom Ekman layer, Journal of Fluid Mechanics, 590, 331–354, https://doi.org/10.1017/S0022112007008087, 2007.

Türk, M. and Emeis, S.: The dependence of offshore turbulence intensity on wind speed, Journal of Wind Engineering and Industrial Aerodynamics, 98, 466–471, https://doi.org/10.1016/j.jweia.2010.02.005, 2010.

van der Laan, M. P. and Sørensen, N. N.: Why the Coriolis force turns a wind farm wake clockwise in the Northern Hemisphere, Wind Energy Science, 2, 285–294, https://doi.org/10.5194/wes-2-285-2017, 2017.

Veers, P., Dykes, K., Basu, S., Bianchini, A., Clifton, A., Green, P., Holttinen, H., Kitzing, L., Kosovic, B., Lundquist, J. K., Meyers, J., O'Malley, M., Shaw, W. J., and Straw, B.: Grand Challenges: wind energy research needs for a global energy transition, Wind Energy Science, 7, 2491–2496, https://doi.org/10.5194/wes-7-2491-2022, 2022.

https://doi.org/10.5194/wes-2026-208
Preprint. Discussion started: 5 November 2026
© Author(s) 2026. CC BY 4.0 License.

Wallace, J. M. and Hobbs, P. V.: Atmospheric Science: an Introductory Survey, Elsevier Academic Press, second edn., ISBN 0-08-049953-8, 2006.

Wu, K. L. and Porté-Agel, F.: Flow Adjustment Inside and Around Large Finite-Size Wind Farms, Energies, 10, 2164, https://doi.org/10.3390/en10122164, 2017.

Wu, Y.-T. and Porté-Agel, F.: Large-eddy simulation of wind-turbine wakes: evaluation of turbine parametrisations, Boundary-Layer Meteorology, 138, 345–366, https://doi.org/10.1007/s10546-010-9569-x, 2011.

Wu, Y.-T. and Porté-Agel, F.: Atmospheric turbulence effects on wind-turbine wakes: An LES study, Energies, 5, 5340–5362, https://doi.org/10.3390/en5125340, 2012.

Wyngaard, J. C.: Turbulence in the Atmosphere, Cambridge University Press, ISBN 9780511840524, 2010.

Zormpa, M., Zilic de Arcos, F., Chen, X., Vogel, C. R., and Willden, R. H.: The effect of flow sampling on the robustness of the actuator line method, Wind Energy, 28, e2965, https://doi.org/10.1002/we.2965, 2025.